



Gas-phase ion chemistry within the photodetachment-modulated electron capture detector
by Kyle Scott Strode

A thesis submitted in partial fulfillment of the requirements for the degree of Doctor of Philosophy in
Chemistry

Montana State University

© Copyright by Kyle Scott Strode (1993)

Abstract:

The objective of this thesis is to expand the utility of the photodetachment-modulated electron capture detector (PDM-ECD) for the study of gas-phase ion chemistry (GPIC) at atmospheric pressure. Specifically, studies of electron photodetachment (PD), a unique electron capture (EC) reaction and two gas-phase ion-molecule reactions at atmospheric pressure are reported.

In the PDM-ECD, p-benzoquinone and its methylated derivatives undergo optical enhancement of EC (OEEC) during irradiation by ultraviolet light. The molecular anions of the quinones also undergo PD over the same wavelength range. A method is described in which the OEEC and PD spectra can be independently measured without interference from each other. The OEEC and PD spectra are reported and compared with solution-phase absorption spectra. From mass spectrometric experiments, the OEEC response is attributed to EC by photochemically produced dimers of the quinones.

By comparison of the PD spectra for I⁻ under dry conditions and with a few torr of water added to the detector gas, the onset for PD from I⁻(H₂O) is shown to occur at a photon energy greater than that for I⁻ by an amount equal to the enthalpy of solvation. The equilibrium constant for the clustering reaction is calculated at 130°C from comparisons of PD responses under dry and wet conditions.

It is shown that gas-phase S_N2 displacement will occur at atmospheric pressure in the PDM-ECD between an alkyl bromide (RBr) and Cl⁻. Chromatographic introduction of RBr is important for separating impurities from the compound of interest. The PD response to Br⁻ produced by the reaction is induced by 365 nm light from a Hg/Xe lamp. A method is shown whereby measuring the PD response at different concentrations of RBr gives information that can be used to determine the second-order rate constant for S_N2 displacement, K_{SN2}, between RBr and Cl⁻. The values for K_{SN2} are reported for 18 alkyl bromides and compared with previously reported gas- and solution-phase results. The temperature dependence of K_{SN2} from 100-200°C is reported for bromomethane and 2-bromopropane.

GAS-PHASE ION CHEMISTRY WITHIN
THE PHOTODETACHMENT-MODULATED
ELECTRON CAPTURE DETECTOR

by

Kyle Scott Strode

A thesis submitted in partial fulfillment
of the requirements for the degree

of

Doctor of Philosophy

in

Chemistry

MONTANA STATE UNIVERSITY
Bozeman, Montana

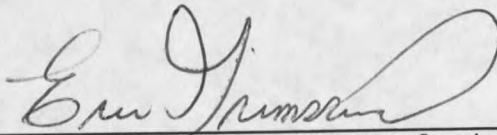
April 1993

D378
St872

APPROVAL
of a thesis submitted by
Kyle Scott Strode

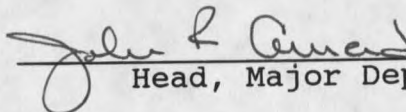
This thesis has been read by each member of the thesis committee and has been found to be satisfactory regarding content, English usage, format, citations, bibliographic style, and consistency, and is ready for submission to the College of Graduate Studies.

3/31/93
Date


Chairperson, Graduate Committee

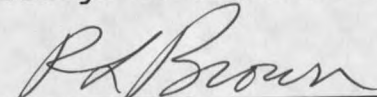
Approved for the Major Department

3-30-93
Date


Head, Major Department

Approved for the College of Graduate Studies

3/31/93
Date


Graduate Dean

STATEMENT OF PERMISSION TO USE

In presenting this thesis in partial fulfillment of the requirements for a doctoral degree at Montana State University, I agree that the Library shall make it available to borrowers under rules of the Library. I further agree that copying of this thesis is allowable only for scholarly purposes, consistent with "fair use" as prescribed in the U.S. Copyright Law. Requests for extensive copying or reproduction of this thesis should be referred to University Microfilms International, 300 North Zeeb Road, Ann Arbor, Michigan 48106, to whom I have granted "the exclusive right to reproduce and distribute my dissertation for sale in and from microform or electronic format, along with the right to reproduce and distribute my abstract in any format in whole or in part."

Signature Kyle Stroh
Date 3-31-93

ACKNOWLEDGEMENT

I would like to thank several past and present members of the research group, especially Dr. Berk Knighton, Dr. Joe Sears and Dr. Steve Mock. I am indebted to them for their helpful suggestions and assistance and for meaningful discussions of the chemistry reported here. I thank all of the members of the research group for help and advice along the way and especially for their friendship. I am grateful to my advisor, Dr. Eric Grimsrud, for his support of my research and for fostering an environment in which I gained a full and mature understanding of chemistry.

I thank my whole family for their moral support, especially my mom and dad for providing an inspiring scholastic example and for nurturing my interest in science. Lastly, I deeply thank Julie for her profound love and support.

TABLE OF CONTENTS

	Page
INTRODUCTION	1
Gas-Phase Ion Chemistry	1
The PDM-ECD	3
Use of the PDM-ECD for Studies of GPIC	7
THEORY	11
Collision Frequency and Thermalization Within the PDM-ECD	11
Reactions Within the Cell	12
Equilibrium Within the PDM-ECD	17
EXPERIMENTAL	19
The PDM-ECD Setup	19
The ECD	20
Sample Introduction	20
Calculation of Sample Concentration Within the PDM-ECD	22
Doping of the Make-Up Gas	23
Optical System	27
Signal Processing	29
Measurement of PD Spectra	32
Setup of the APIMS	32
Ion Source	34
Optical System	34
Quadrupole	35
Sample Introduction	35
RESULTS AND DISCUSSION	36
Gas-Phase Photochemistry of Quinone Molecules and Their Molecular Anions	36
Description of the Problem	37
Characterization of OEEC Using the PDM-ECD	39
Temperature Dependence of EC Response	40
Lack of OEEC for $C_{12}H_{26}$ and $C_{18}H_{38}$	42
Dependence of OEEC on Concentration	43
Characterization of OEEC Using a Chopped Light Beam	46
Method For Independent Measurement of OEEC and PD	55

TABLE OF CONTENTS-Continued

	Page
PD Spectra of the Quinone Molecular Anions	57
Direct Photodetachment	59
Resonance Photodetachment	62
OEEC Spectra of the Quinones	64
Characterization of OEEC Using APIMS	68
Elucidation of the Mechanism	
Responsible for OEEC	74
Possible Structures of the Dimers	81
PDM-ECD Study of Iodide-Water	
Clustering Equilibria	83
Response of PDM-ECD to Iodide	
With Water Present	84
Relative Abundances of Iodide-Water Clusters	
From PDM-ECD Measurements	87
Determination of Equilibrium Constants and	
Thermochemical Data for the Iodide-Water	
Clustering Reaction	90
Comparison of the PD Spectra of I^-	
Under Dry and Wet Conditions	91
Determination of ΔH From PD Spectra	94
Kinetics of Gas-Phase S_N2 Reactions of	
Alkyl Bromides With Chloride	95
Introduction of Reactants and Monitoring	
of S_N2 Displacement	97
Experimental Measurement of S_N2 Displacement	99
Derivation of S_N2 Rate Law	103
Procedure for Measurement	
of S_N2 Rate Constants	105
Results of Rate Constant Measurements	107
Saturated Alkyl Bromides	108
Unsaturated Compounds	123
Temperature Dependence of S_N2 Rate Constants	126
SUMMARY	130
LITERATURE CITED	137

LIST OF TABLES

Table	Page
1. Photodetachment thresholds of the quinone anions .	60
2. EC rate coefficients for the quinone molecules . .	81
3. Rate constants and relative reactivities for RBr + Cl ⁻ ---> RCl + Br ⁻	112
4. Rate constants for reactions of BM and 2BPR with Cl ⁻ from 100° to 200°	128
5. Values from Arrhenius plots of rate constants for reactions of bromomethane and 2-bromopropane with Cl ⁻	128

LIST OF FIGURES

Figure	Page
1. Apparatus used for the PDM-ECD studies	19
2. Gaussian peak model used for calculation of sample concentration within the ECD	24
3. Configuration of the make-up gas line to allow for addition of dopants to the cell	26
4. Emission spectra of the Xe and Hg/Xe arc lamps	28
5. Circuit diagram for the pulser and electrometer used for the PDM-ECD	30
6. Apparatus used for APIMS studies	33
7. Electron capture detector responses to 200 ng of 200 ng of <i>p</i> -benzoquinone through repeated GC analyses of a standard solution while varying the conditions of the cell irradiation	38
8. Electron capture detector responses to 200 ng of <i>p</i> -benzoquinone through repeated GC analyses while varying the temperature of the cell without irradiation	41
9. Response of the PDM-ECD to varying concentrations of <i>p</i> -benzoquinone with and without irradiation	44
10. Response enhancement of the PDM-ECD observed with light of 240 nm and at varying concentrations of <i>p</i> -benzoquinone	45
11. GC analysis of <i>p</i> -benzoquinone with chart paper speed of 1 cm sec ⁻¹ and with 240 nm light chopped at 0.5 Hz	48
12. Graph used to calculate the time constant for the rate of change of the chemical system within the ECD at three different flow rates	51
13. Simulation of the two waveforms sent to the lock-in amplifier and the phase angle offset used to achieve the maximum negative output	54
14. Electron photodetachment spectra of the quinone molecular anions	58

LIST OF FIGURES-Continued

Figure	Page
15. Optically enhanced electron capture spectra of the quinones	66
16. Condensed-phase absorption spectra of the quinone molecules	67
17. Negative ion atmospheric pressure ionization mass spectra of <i>p</i> -benzoquinone with and without irradiation by 240 nm light	71
18. Superimposed single ion chromatograms for $m/z = 108$ and $m/z = 216$ from APIMS	72
19. Negative ion atmospheric pressure ionization mass spectra of <i>p</i> -benzoquinone recorded before and after abruptly extinguishing the light	73
20. Possible structures of the dimers of <i>p</i> -benzoquinone and 2,6-dimethyl- <i>p</i> -benzoquinone	82
21. PDM-ECD chromatograms of CH_3I with and without 3.9 torr water at 130°C and with 380 nm light	85
22. Relative abundances in the PDM-ECD of I^- and $\text{I}^-(\text{H}_2\text{O})_n$ from 130 - 190°C with 3.9 torr water present in the detector gas	89
23. Electron photodetachment spectra of I^- at 100°C under dry conditions and with 1.9 torr water present in the detector gas	92
24. Response of the PDM-ECD to 1-bromobutane chromatographically introduced to the detector with Cl^- continuously present	100
25. Plot of the magnitudes of $\text{S}_{\text{N}}2$ responses as a function of the concentration of bromoethane in the detector at the peak maxima	102
26. Response of the PDM-ECD to different concentrations of 1-bromobutane with Cl_- present	106
27. Plots of ECD concentrations of RBr vs. $[\text{Br}^-]/[\text{Cl}^-]$ for six primary unsubstituted saturated alkyl bromides	109

LIST OF FIGURES-Continued

Figure		page
28.	Plots of ECD concentrations of RBr vs. $[\text{Br}^-]/[\text{Cl}^-]$ for three primary substituted and three secondary saturated alkyl bromides	110
29.	Plots of ECD concentrations of RBr vs. $[\text{Br}^-]/[\text{Cl}^-]$ for six primary unsaturated alkyl bromides	111
30.	Reaction coordinate for the $\text{S}_{\text{N}}2$ displacement reaction of Cl^- with RBr where $\text{R} = \text{CH}_3$	117
31.	Arrhenius plots of rate constants for bromomethane and 2-bromopropane between 100 and 200°C	129

ABSTRACT

The objective of this thesis is to expand the utility of the photodetachment-modulated electron capture detector (PDM-ECD) for the study of gas-phase ion chemistry (GPIC) at atmospheric pressure. Specifically, studies of electron photodetachment (PD), a unique electron capture (EC) reaction and two gas-phase ion-molecule reactions at atmospheric pressure are reported.

In the PDM-ECD, *p*-benzoquinone and its methylated derivatives undergo optical enhancement of EC (OEEC) during irradiation by ultraviolet light. The molecular anions of the quinones also undergo PD over the same wavelength range. A method is described in which the OEEC and PD spectra can be independently measured without interference from each other. The OEEC and PD spectra are reported and compared with solution-phase absorption spectra. From mass spectrometric experiments, the OEEC response is attributed to EC by photochemically produced dimers of the quinones.

By comparison of the PD spectra for I^- under dry conditions and with a few torr of water added to the detector gas, the onset for PD from $I^-(H_2O)$ is shown to occur at a photon energy greater than that for I^- by an amount equal to the enthalpy of solvation. The equilibrium constant for the clustering reaction is calculated at 130°C from comparisons of PD responses under dry and wet conditions.

It is shown that gas-phase S_N2 displacement will occur at atmospheric pressure in the PDM-ECD between an alkyl bromide (RBr) and Cl^- . Chromatographic introduction of RBr is important for separating impurities from the compound of interest. The PD response to Br^- produced by the reaction is induced by 365 nm light from a Hg/Xe lamp. A method is shown whereby measuring the PD response at different concentrations of RBr gives information that can be used to determine the second-order rate constant for S_N2 displacement, k_{SN2} , between RBr and Cl^- . The values for k_{SN2} are reported for 18 alkyl bromides and compared with previously reported gas- and solution-phase results. The temperature dependence of k_{SN2} from 100-200°C is reported for bromomethane and 2-bromopropane.

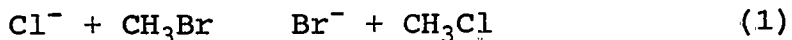
INTRODUCTION

Gas-Phase Ion Chemistry

In the 1960's, mass spectrometric methods were developed which allowed scientists to study the behavior of ions in the gas phase under controlled conditions. Although ions are produced and controlled easily in the condensed phase, the electrostatic interactions with the solvent often have a pronounced effect on the dynamics, energetics and mechanism of an ionic reaction (1). In the gas phase, the presence of solvent can be eliminated or carefully controlled, and the intrinsic properties of ions and molecules can be studied (2). During the last 30 years, research in gas-phase ion chemistry (GPIC) has had a profound impact on a wide variety of scientific disciplines. Scientists have discovered important information about the ion-molecule reactions that occur in the earth's atmosphere (3) and in interstellar space (4). GPIC research has helped in the development of highly sensitive methods for chemical analysis, and in the evolution of useful theoretical methods for calculating and predicting chemical reactivity (5).

Nearly all of the instrumental techniques used to study GPIC employ a mass spectrometer (MS) for detection and measurement of ions. Among the most widely used of the MS-based techniques are ion cyclotron resonance (ICR), flowing afterglow (FA), selected ion flow tube (SIFT), time-of-flight (TOF), and pulsed e-beam high pressure mass spectrometric (PHPMS) methods. Because of the nature of ion containment and detection in a mass spectrometer, the above methods require that ionic reactions be studied at relatively low total pressures; ICR operates at 10^{-5} - 10^{-6} torr, while the other methods require pressures between 0.5 and 6 torr (6). Instrumental difficulties have for the most part prevented investigations above these pressures. However, in several recent articles (6-13), Grimsrud et al. have reported initial studies of GPIC at atmospheric pressure. The most important reason for undertaking research at atmospheric pressure was the need to understand GPIC under all physical conditions in which reactions occur.

The importance of measurements over a wide range of pressures is illustrated by the simple bimolecular nucleophilic displacement (S_N2) reaction shown below.



This reaction has been studied by ICR at about 10^{-6} torr

(5), by PHPMS (14), FA (15) and SIFT (16) at about 1 torr, and by kinetic ion mobility mass spectrometry (KIMMS) (6) at 640 torr. The rate constant for Reaction 1 at 300 K varies from $1.2 \times 10^{-11} \text{ cm}^3 \text{ s}^{-1}$ by ICR to 2.3, 2.1, and $2.7 \times 10^{-11} \text{ cm}^3 \text{ s}^{-1}$ by PHPMS, FA, and SIFT, respectively. At 400 K, the rate constant measured by PHPMS is $8.8 \times 10^{-12} \text{ cm}^3 \text{ s}^{-1}$ and by KIMMS it is $3.4 \times 10^{-11} \text{ cm}^3 \text{ s}^{-1}$. Riveros et al. (1), Bohme et al. (17) and Caldwell et al. (14) attribute the low value of the ICR measurement at 300 K to the large difference in pressure between ICR and the measurements at near 1 torr. The same conclusion was drawn by Giles and Grimsrud (6) with respect to the PHPMS and KIMMS measurements at 400 K. For systems like Reaction 1, changes in pressure are thought to have a significant effect on reaction dynamics. For other systems, like the analogous S_N2 reaction between Cl^- and $\text{CH}_3(\text{CH}_2)_2\text{CH}_2\text{Br}$, the rate constant is thought to be relatively independent of pressure (6). Obviously, there is a need for more measurements of reaction dynamics and energetics at much higher pressures so that scientists can gain a more complete understanding of GPIC.

The PDM-ECD

In 1988, Mock and Grimsrud introduced the photodetachment-modulated pulsed electron capture detector

(PDM-ECD), and demonstrated its utility for the trace analysis of halocarbon mixtures (18). In subsequent reports, it was shown that the PDM-ECD could be used for the study at atmospheric pressure of many GPIC processes. The PD spectra of the radical anions of 31 nitroaromatic compounds were reported for the first time (10), along with the PD spectra of the radical anions of azulene (11), SF₆ and several perfluorinated compounds (12). In some cases, these spectra were compared with the known condensed-phase absorption spectra of the anions and found to be quite similar. The instrument was shown to be useful for kinetic study when it was used to measure the thermal electron detachment rate constants for azulene (11). The PDM-ECD was also shown to be useful for determining the relative amounts of Cl⁻ and Br⁻ produced by dissociative EC from CBrCl₃ (9). Finally, experiments revealed that *p*-benzoquinone and its methylated derivatives undergo optically enhanced electron capture (OEEC) in the PDM-ECD (19, 20).

The utility of the PDM-ECD for the study of GPIC derives from several factors. First, negative ions are easily generated in the instrument by dissociative electron capture (EC), Reaction 2, or by resonance EC,



Reaction 3. A second advantage of the PDM-ECD involves the ubiquitous presence of sample impurities. In the study of many GPIC processes, such as slow ion-molecule reactions, trace contaminants can cause fast side reactions to occur that completely overwhelm the reaction of interest. As a result, researchers must take great pains to ensure the purity of their samples (6, 14-16, 21). Occasionally, simple reactions are impossible to study because of the presence of contaminants (14). Impurities are not a problem with the PDM-ECD. The instrument has a built-in "immunity" toward contaminants because "dirty" neutral reactants and negative ion precursors can be introduced to the PDM-ECD with chromatographic separation from potential impurities. A third advantage of the PDM-ECD results from its use of electron photodetachment (PD), Reaction 4, as an induced



perturbation of the ECD signal. Along with the normal EC response of the PDM-ECD, PD provides additional specificity for detection of many compounds. These compounds must capture thermalized electrons by Reaction 2 or 3, and the resulting negative ions must undergo PD by light of a chosen wavelength (22). In addition to simply providing additional response specificity, PD is a well-established method for studying negative ion

thermochemistry, spectroscopy and kinetics. Electron affinities (23-25), bond dissociation energies (26, 27), and solvation energies (28-31) have been determined by PD, along with energies of electronic transitions in negative ions (23). A final advantage of the PDM-ECD is that it operates at atmospheric pressure. In the example of the S_N2 reaction given above, research at atmospheric pressure was shown to be important to a more complete fundamental understanding of GPIC. In addition to simply increasing theoretical knowledge, research at atmospheric pressure using the PDM-ECD allows for unambiguous study of electron photodetachment spectroscopy. In the past, PD measurements have usually been made by the ICR technique. Anions formed in the ICR usually possess an excess of internal energy due to the processes by which they are formed. This excess internal energy is not removed efficiently by collisions at the operating pressures of the ICR (10^{-6} - 10^{-5} torr), and this can make the interpretation of PD spectra complicated (23). In addition, if the initially-formed excited anions possess lifetimes against autodetachment that are too short, PD cannot compete with autodetachment, because stabilizing collisions are too infrequent at the low pressure of the ICR (10). These problems are avoided in the atmospheric pressure environment of the PDM-ECD. The frequent

collisions that occur at atmospheric pressure guarantee that all species are in thermal equilibrium with one another and that negative ions will be in their ground electronic and lowest vibrational states (10).

Despite its many advantages, the PDM-ECD has several distinct drawbacks for the study of GPIC. Many negative ions of experimental interest that can be produced in other instruments cannot be generated in the PDM-ECD by resonance or dissociative EC. A related problem is that for some systems, the neutral reactants are rapidly destroyed in the PDM-ECD by one of the same two EC reactions. This limits the number of experimental systems amenable to study by the PDM-ECD.

Use of the PDM-ECD for Studies of

Gas-Phase Ion Chemistry

The past success of the PDM-ECD for a variety of investigations, along with its known advantages and disadvantages, suggest that the instrument should be useful for further study of gas-phase ion chemistry. The following work describes the utility of the PDM-ECD for detailed and fundamental investigations of GPIC. These studies are divided into three major areas: 1) quinone photochemistry, 2) iodide-water clustering equilibria, and 3) kinetics of S_N2 reactions.

The continued measurement of PD spectra for many more molecular anions is important for the reasons given above. These PDM-ECD measurements are fairly straightforward for most systems. However, in the case of the molecular anions of quinones, PD measurements are complicated by the simultaneous occurrence of optically enhanced electron capture. As it was mentioned previously, the observation of OEEC was reported recently by Mock and Grimsrud (19, 20). Further investigations using the PDM-ECD will be important to a more complete understanding of the photochemistry regarding OEEC and PD by the quinones.

Ion-molecule reactions are one area of GPIC which has not been fundamentally investigated by the PDM-ECD. In two recent reports (32, 33), Grimsrud et al. developed a second-generation version of the PDM-ECD for simple iodide- and bromide-specific detection based on PD and ion-molecule clustering. Although this early research focused on the analytical applications of clustering reactions in the PDM-ECD, the potential of the instrument for fundamental studies of a variety of ion-molecule reactions was clearly demonstrated.

Negative ion clustering equilibria are perfectly amenable to fundamental study, at atmospheric pressure by the PDM-ECD. One of the problems traditionally associated with the study of ion clustering equilibria at high

pressures is that in the measurement and detection of the clusters, the established equilibrium may be disturbed. This can be especially problematic in mass spectrometric sampling from ion sources in which the pressure exceeds about 10 torr (7, 34). The PDM-ECD should be useful for the study of negative ion clustering equilibria even though it operates at atmospheric pressure. No significant perturbation of equilibrium will occur because the measurement of ions by PD takes place within the ionization volume itself, without sampling into a region of lower pressure. For the PDM-ECD study of negative ion clustering equilibria, it is only necessary that the free and clustered anions possess distinct PD spectra. An initial study of the negative ion clustering reaction between iodide and water will be investigated by the PDM-ECD. This investigation of iodide-water clustering is important because it can provide a model for future PD studies of clustering by the PDM-ECD and by other methods.

Bimolecular nucleophilic displacement is another simple ion-molecule reaction that can be studied by the PDM-ECD. It is clear from the earlier discussion of the reaction between Cl^- and CH_3Br that there is important fundamental knowledge, especially in the area of kinetics, to be gained by the study of $\text{S}_{\text{N}}2$ reactions at atmospheric pressure. For the study of $\text{S}_{\text{N}}2$ reactions by the PDM-ECD,

all that is necessary is that the PD spectra of the reagent and product ions be distinguishable. The reactions of alkyl bromides with chloride are well-suited for this type of study by the PDM-ECD. The PD spectra of Cl^- and Br^- are different, and the reactions between Cl^- and a few alkyl bromides have recently been characterized by other methods (6, 14, 16).

THEORY

Collision Frequency and ThermalizationWithin the PDM-ECD

As it was discussed in the Introduction, the dynamics of gas-phase processes near atmospheric pressure differ significantly from those at lower pressures. For a thorough understanding of the PDM-ECD, it is therefore important to predict how increased pressure will affect gas-phase ion chemistry.

The fundamental difference between GPIC at atmospheric pressure and at lower pressures has to do with collision frequency, z . The value for z at a particular pressure may be calculated from Equation 5, where \bar{v} is the

$$z = \bar{v}\sigma\sqrt{2}\frac{N}{V} \quad (5)$$

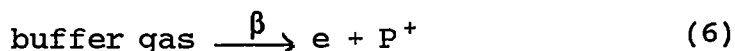
mean velocity of the particles and N/V is their number density. The term, σ , is the collision cross-section and is calculated from $\sigma = 2\pi r^2$ where r is the radius of the particles (35). Using this equation, the calculated collision frequency at 640 torr and 125°C is $\sim 7 \times 10^9$ sec⁻¹. GPIC is often studied in the one torr range by PHPMS and FA methods, and by ICR at 10⁻⁵ torr. At one

torr the value for z is smaller than at atmospheric pressure by about three orders of magnitude, while in the 10^{-5} torr ICR cavity, z is incredibly low, $\sim 100 \text{ sec}^{-1}$.

The most important result of the high collision frequency at atmospheric pressure is that excited ions and molecules are rapidly stabilized and brought into thermal equilibrium with the buffer gas (36). As it was mentioned in the Introduction, this is important because ionization processes and energetic ion-molecule reactions often produce excited species that contain substantial internal energy. Meot-Ner concluded that for a variety of ion/buffer gas systems, vibrationally excited ions are generally thermalized in about 10 collisions, and a Boltzmann temperature distribution is attained after about 100 collisions (37). Therefore, from the collision frequencies determined above, collisional stabilization at atmospheric pressure takes place in about 1 nsec, which easily allows for the thermal study of even the fastest ionic reactions.

Reactions Within the Cell

The production of ions in the PDM-ECD cell volume begins with Reaction 6, in which the buffer gas is ionized



by beta particles emitted from a ^{63}Ni -on-Pt foil. The rate constant for this reaction is β . The foil used has an activity, A , of 8 mCi (3×10^8 disint sec^{-1}), and the average energy of a beta particle, E_β , is 17 keV. Using these numbers, a value of $\beta = 7 \times 10^{10}$ ion pairs sec^{-1} is calculated from Equation 7, where 35 eV is the amount of

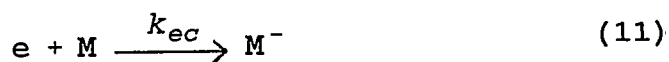
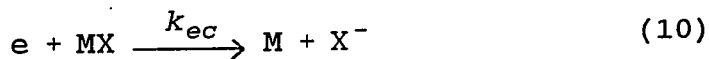
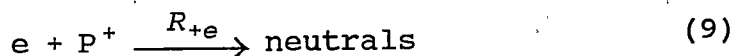
$$\beta = \frac{\frac{1}{2} AE_\beta}{35\text{eV}} \quad (7)$$

energy required from the beta particle to produce one ion pair. The average electron density in the cell, $[e]$, can then be calculated from Equation 8, where V_o is the cell

$$[e] = \sqrt{\frac{\beta}{V_o R_{+e}}} \quad (8)$$

volume and the positive ion-electron recombination rate constant is given by $R_{+e} = 3 \times 10^{-6} \text{ cm}^3 \text{ sec}^{-1}$ (38). With a 2.65 cm^3 cell volume, the electron density is calculated to be $9 \times 10^7 \text{ cm}^{-3}$. The electron density in the cell is continuously monitored by collecting the electrons at positively-charged pin that is pulsed at a fixed frequency.

Once formed, the thermal electrons can interact with species present in the cell by Reactions 9-11.

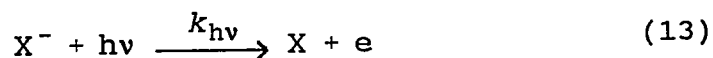
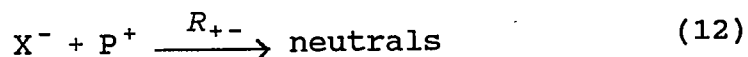


The recombination of positive ions with electrons is shown in Reaction 9. The pseudo first-order rate constant, R_{+e} , is calculated from the above values to be 270 sec^{-1} .

Reactions 10 and 11 are dissociative and resonance electron capture, respectively. One of these reactions will occur when a molecule with a high electron affinity enters the cell. Dissociative electron capture leads to formation of an atomic negative ion, while resonance electron capture forms the molecular anion. In the case of resonance electron capture, it is important to note that the reaction is actually a two step process. First, the molecule captures an electron to form the excited molecular anion, M^{-*} . In order to form a stable molecular anion, this species then undergoes a rapid series of collisions with the buffer gas (as described in the previous section) which collisionally stabilize the anion and bring it into thermal equilibrium with the other gas molecules. Electron capture (EC) by either the dissociative or resonance method causes a decrease in the

average electron density within the cell, and a concomitant decrease in the monitored response at the positively pulsed pin.

Negative ions are destroyed by Reactions 12 and 13.

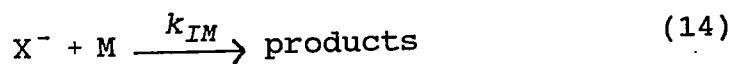


In the absence of light, negative ions will be lost almost exclusively by ion-ion recombination, Reaction 12. Although a few ions are also lost by diffusion to the walls, Zook (36) determined that the first-order rate constant for this process is only about 5 sec^{-1} for a cell of similar size. Ventilation of ions from the cell is also insignificant in the PDM-ECD, as the value is less than 1 sec^{-1} . $R_{+-}[P^+]$ is the pseudo first-order rate constant for ion-ion recombination. The value for $R_{+-}[P^+]$ has been estimated by Mock and Grimsrud (18) to be equal to $100 \pm 50 \text{ sec}^{-1}$ for the PDM-ECD instrument. It is thought to be independent of the identity of the EC-active species (18) and independent of temperature (11).

If a negative ion is formed during irradiation of the cell, electron photodetachment (PD), Reaction 13, may occur. For this reaction to take place, the photon energy must be greater than the electron affinity of the

corresponding neutral. Reaction 13 returns a bound electron to the continuum, to be collected at the pin. The original electron capture event is therefore not detected by the instrument if Reaction 13 occurs. The pseudo first-order rate constant, k_{hv} , depends on the photon flux through the cell and on the PD cross-section of the negative ion. Even though the experimental values for k_{hv} are smaller than $R_{+}[P+]$, Mock and Grimsrud found that they could easily monitor PD by passing a chopped light beam through the cell and measuring the resulting perturbation by the method described in Experimental (18).

Before it is destroyed, a negative ion can react with a neutral in the PDM-ECD and undergo an ion-molecule reaction, as shown in Reaction 14. In this type of



reaction, the products might be species such as clustered ions or exchange products. In many reactions of this type, products are formed at nearly every collision between the ion and the neutral. These reactions are said to be collisionally limited. The Langevin/ADO collision rate constant, k_c , corresponds to this second-order process of unit efficiency. It has a value of about 10^{-9} $\text{cm}^3 \text{sec}^{-1}$, and can be calculated for a specific system

from Equation 15 (39) with parameters from several sources (39-41).

$$k_c = \frac{2\pi q}{\mu^{1/2}} \left[\alpha^{1/2} + c\mu_D \left(\frac{2}{\pi KT} \right)^{1/2} \right] \quad (15)$$

q = charge = 4.8×10^{-10} esu
 μ = reduced mass
 α = polarizability of molecule (ref. 41)
 c = dipole locking constant (ref. 39)
 K = Boltzmann's constant = 1.38×10^{-16} erg
 T = absolute temperature = 398 K

Equilibrium Within the PDM-ECD

Kebarle has listed three criteria that are necessary for the establishment of ionic equilibrium in the gas phase. First, the reactants must be in thermal equilibrium with the surroundings. Second, the ions that are involved in the equilibrium must be coupled by reactions that are faster than all other processes that affect their concentrations. Third, the system must be allowed enough time to reach equilibrium (42).

The three criteria listed above are met in the PDM-ECD. In a previous section, it was demonstrated that thermalization readily occurs at atmospheric pressure in the PDM-ECD ionization volume. Krieger and Grimsrud have shown that at atmospheric pressure, equilibrium is attained extremely quickly in comparison with the

competing processes of ion-ion recombination, ventilation from the cell and diffusion (43). Finally, in the PDM-ECD, the pulsing of the pin is responsible for collecting the electrons in the cell and monitoring the course of ionic reactions. The typical pulsing period of 200 μ s is far longer than the lifetime of an ion (43) involved in a typical gas-phase ionic reaction at equilibrium.

EXPERIMENTAL

PDM-ECD Setup

A schematic representation of the PDM-ECD setup is shown in Figure 1. The following sections describe the experimental considerations associated with each aspect of the system.

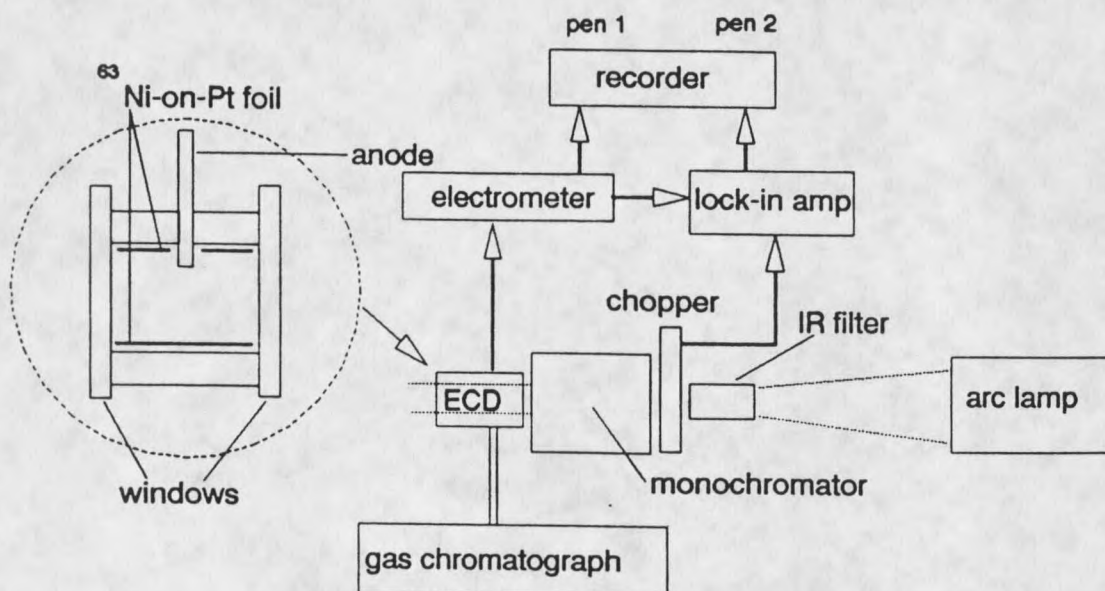


Figure 1. Apparatus used for PDM-ECD studies.

The ECD

The ECD was constructed from a solid block of stainless steel with a central cylindrical cavity. The walls of the cavity were formed by a ^{63}Ni -on-Pt foil of 9 mCi activity. The cavity was 2.0 cm long and 1.3 cm wide, which resulted in an ionization volume of 2.65 cm³. Fused silica windows form the front and rear walls of the cavity and allow for light to enter the ionization volume. They were sealed with teflon washers. The external transmittance of these windows reaches 90% at 220 nm and remains constant until nearly 1.5 μ . The operating temperature range of the ECD was from room temperature to 200°C. The temperature was regulated by a Watlow temperature controller equipped with two cartridge heaters and a thermocouple feedback control. A stainless steel pin with a diameter of $1/16$ in. served as the anode. It entered the ECD from the side through a teflon plug and protruded $1/8$ in. into the ionization volume. The pressure within the ECD was approximately 640 torr (atmospheric pressure in Bozeman) for all experiments.

Sample Introduction

The halocarbons and quinones were obtained from commercial suppliers and were used without further purification since the GC provided adequate separation of

the desired compounds from any potential impurities. For small halocarbons with boiling points less than about 80°C, gas samples were prepared in nitrogen by successive dilution into gas-tight glass vessels. A 4.3 L glass carboy was pressurized to 1150 torr and was used for final storage of the samples. This method allowed numerous aliquots to be transferred by a 30 mL gas-tight syringe to the gas sampling loop. The reproducibility of sample delivery by this method is very good (less than 5% variation) (44). The larger halocarbons were diluted in HPLC-grade hexane to achieve an appropriate concentration. The quinones were diluted in HPLC-grade toluene. Between 0.1 μ L and 1 μ L of these liquid samples were injected onto the GC with a 1 μ L syringe.

Samples were introduced into the PDM-ECD upon elution from a gas chromatograph (GC) (Varian Model 3700). Three different columns and two different injection methods were used. The gaseous samples were introduced to the gas chromatograph by a 2.0 cm³ gas sampling loop (Carle Model 8030). The stainless steel column used was 10-ft \times 1/8 in. and was packed with 10% SF-96 on Chromosorb W. For the quinones and the larger halocarbons with boiling points above 80°C, the liquid samples were introduced to the GC by a heated direct on-column injection port. A wide-bore 3 meter capillary column (Hewlett Packard HP-17:

50% phenyl- and 50% methyl polysiloxane) was used for the quinones. A megabore 15 meter capillary column (Alltech RSL-200: polydiphenyldimethylsiloxane) was used for the larger halocarbons. The carrier and make-up gases were 10% methane in argon for the halocarbons and nitrogen for the quinones. The gases were purified by passage through water- and oxygen-removing traps (Alltech). The flow rates of the carrier and make-up gases were measured separately and were varied along with the column temperature to achieve optimal separation, retention time and chromatographic peak shape for each compound. The chromatographic retention times of all compounds were determined from parallel GC studies with flame ionization detection and/or mass spectrometric detection.

Calculation of Sample Concentration

Within the ECD

For many of the compounds studied, it was necessary to know the concentration of the analyte within the ECD at the time corresponding to the maximum of the chromatographic peak. The calculation of this quantity is facilitated by the gaussian shape of most of the chromatographic peaks. It is well-known that 95.5% of the area of a gaussian peak is contained within 2σ on either side of the maximum (45). It is also known that a triangle drawn with two sides tangent to the inflection

points on the sides of a gaussian peak will intersect the base exactly 2σ on either side of the maximum (46) (see Figure 2). It is therefore easy to locate on a chromatogram the points on the baseline that correspond to -2σ and $+2\sigma$. If a chromatographic peak is gaussian in shape, 95.5% of the analyte mass will have eluted during the time corresponding to 4σ . For a gaussian peak of area = 1, the average magnitude of the curve, \bar{y} , will be given by $0.955/4 = 0.239$, as shown in Figure 2. For a chromatographic peak, the average concentration (in molec mL^{-1}) of the analyte within the ECD, \bar{c} , can be calculated from Equation 16, where # is the number of molecules

$$\bar{c} = \# / WF \quad (16)$$

injected, W is the time width of the base of the triangle as shown in Figure 2, and F is the flow rate in mL sec^{-1} . The magnitude of a gaussian peak at its maximum is 0.3989 (45), and is a factor of 1.67 greater than \bar{y} . Therefore, multiplication of \bar{c} by 1.67 gives the concentration of the analyte within the ECD at the time corresponding to the maximum of the chromatographic peak.

Doping of the Make-up Gas

For the iodide-water clustering experiments, it was necessary to introduce a known partial pressure of water into the ionization volume. This was accomplished by inserting a glass bubbling device into the make-up gas

line after the oxygen- and water-removing traps. The setup of the bubbler in conjunction with the GC is shown in Figure 3. Make-up gas was bubbled through a fritted glass inlet into the enclosed vessel, which contained HPLC-grade water. The bubbler was immersed in a temperature controlled water bath. The water-saturated make-up gas passed through heated transfer lines and was mixed with the effluent from the GC immediately prior to the PDM-ECD. The partial pressure of water in the PDM-ECD was calculated from the temperature of the bubbler and the ratio of make-up gas flow to total flow through the PDM-ECD.

For the S_N2 experiments, it was necessary to introduce a compound to the PDM-ECD that produced unclustered chloride ion following dissociative electron capture in the ionization volume. CF_2Cl_2 (Matheson) was introduced into the PDM-ECD as shown in Figure 3. With an extremely slow flow rate, the compound was introduced continually into the make-up gas line through a needle valve. The introduction of CF_2Cl_2 was controlled so that the normal ECD current (described in Signal Processing) was reduced to half of its undoped value. Under these conditions, the chloride concentration was thought to be approximately equal to that of electrons in the ionization volume.

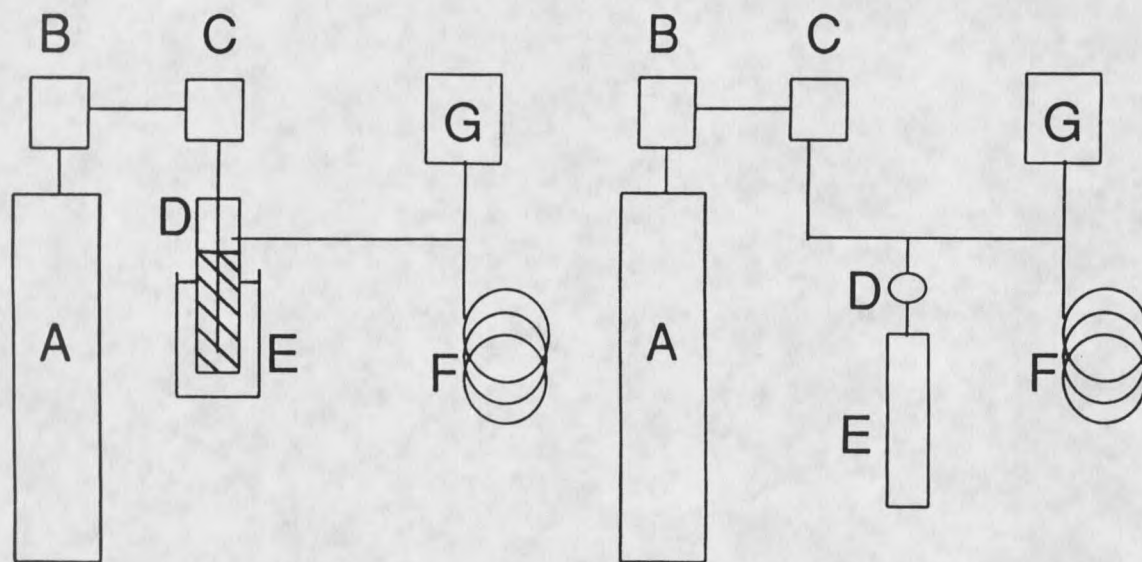


Figure 3.

Configuration of the make-up gas line to allow for addition of dopants to the cell. In both figures, the components are (A) make-up gas source tank, (B) oxygen-removing trap, (C) molecular sieve/water-removing trap, (F) gas chromatograph, and (G) the ECD cell. On the left, (D) is a fritted glass water bubbler and (E) is a constant temperature bath. On the right, (D) is a needle valve controlling the introduction of CF_2Cl_2 from a lecture bottle (E) to the make-up gas.

Optical System

All of the optical components were purchased from Photon Technology International. The optical system included a 1000 Watt Xenon or Hg/Xe arc lamp (Model A5000), an IR water filter, a mechanical light beam chopper (Model 4000), and a grating monochromator (Model 01-002) with a focal length matched to that of the arc lamp. The arc lamp housing contained an elliptical reflector of $f/4$, which focused most of the light into a circular image with a diameter of 1 cm. The focal point was 16 in. in front of the front faceplate of the arc lamp housing. Either of the two lamps can produce up to 105 Watts of total light power (18). From Figure 4 it can be seen that the Xe lamp has a relatively even emission spectrum, while the Hg/Xe lamp has many large emission spikes. The monochromator was positioned so that the entrance slit was at the focal point of the lamp. Both the entrance and exit slits were set to 6.5 mm for the S_N2 experiments and 5 mm for all of the other experiments. This resulted in bandwidths of 26 nm and 20 nm respectively. The monochromator grating had an optimal wavelength of 400 nm, with 1200 lines/mm. The IR water filter was mounted on top of the optical chopper motor and positioned so that the filter exit window was 5 mm from the monochromator entrance slit, and there was sufficient

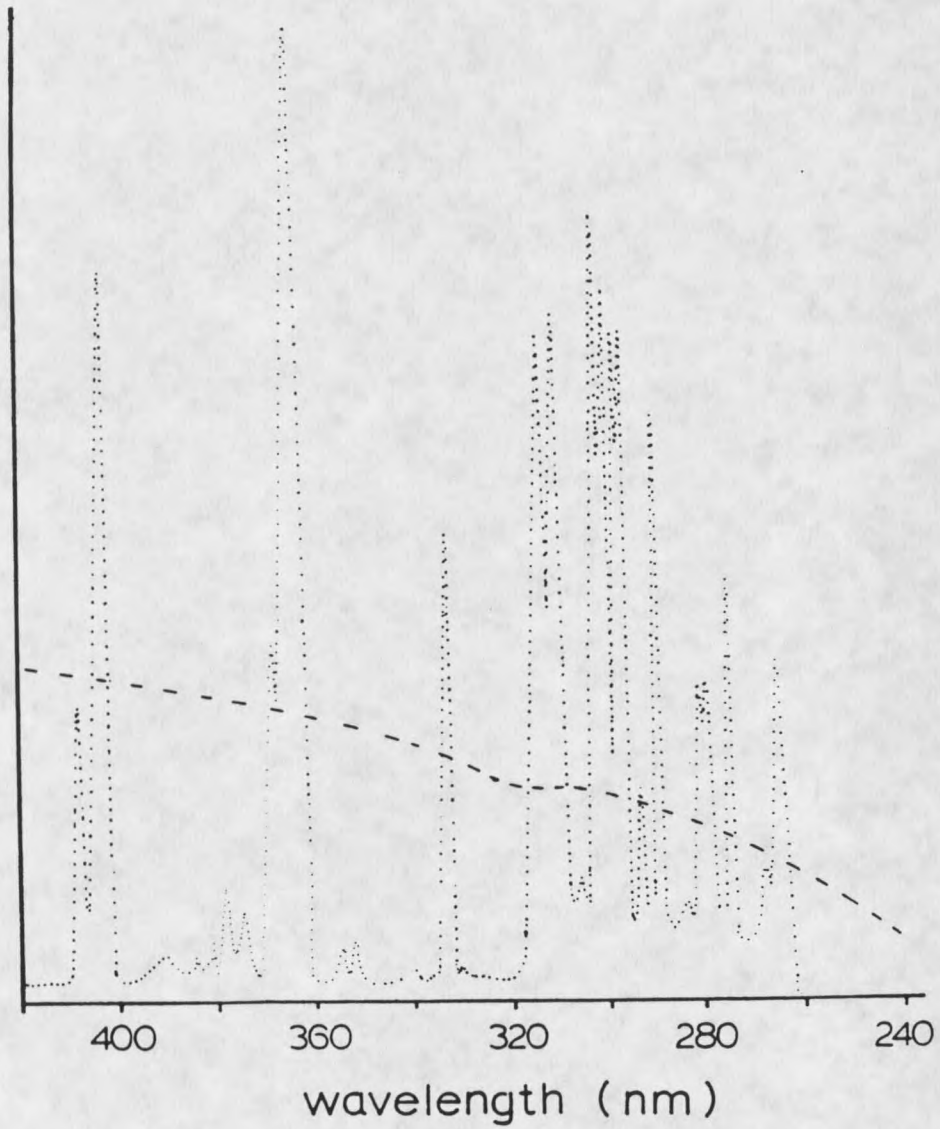


Figure 4. Emission spectra of the Xe (dashed line) and the Hg/Xe (dotted line) arc lamp.

room for rotation of the chopper disk. The frequency of chopping was 23 Hz except for the quinone experiments where it was varied. The on-off nature of the chopped light beam closely resembled a 50/50 duty cycle square wave. For a few experiments, it was necessary to remove the monochromator and focus all of the light into the ionization volume. For these experiments, a light shield was positioned 8 mm in front of the ECD so that stray light would not strike the external surface of the apparatus. A 1.3 cm hole in the shield allowed only focused light to enter the ionization volume. The arc lamp housing was positioned so that the front faceplate was 16 in. from the shield.

After passage through the monochromator, relative light flux, Φ , was measured by a home-built quantum counter (47) which was placed in the position usually occupied by the ECD. The relative quantum efficiency measured by this device is constant over the wavelength range measured. Measurements were made at 10 nm intervals from 200 nm to 600 nm.

Signal Processing

For the control and measurement of the ECD current, a home-built ECD pulser and electrometer were used. The circuit was designed by Grimsrud and Knighton (48) and modified by Mock (44). A diagram of the circuit is shown

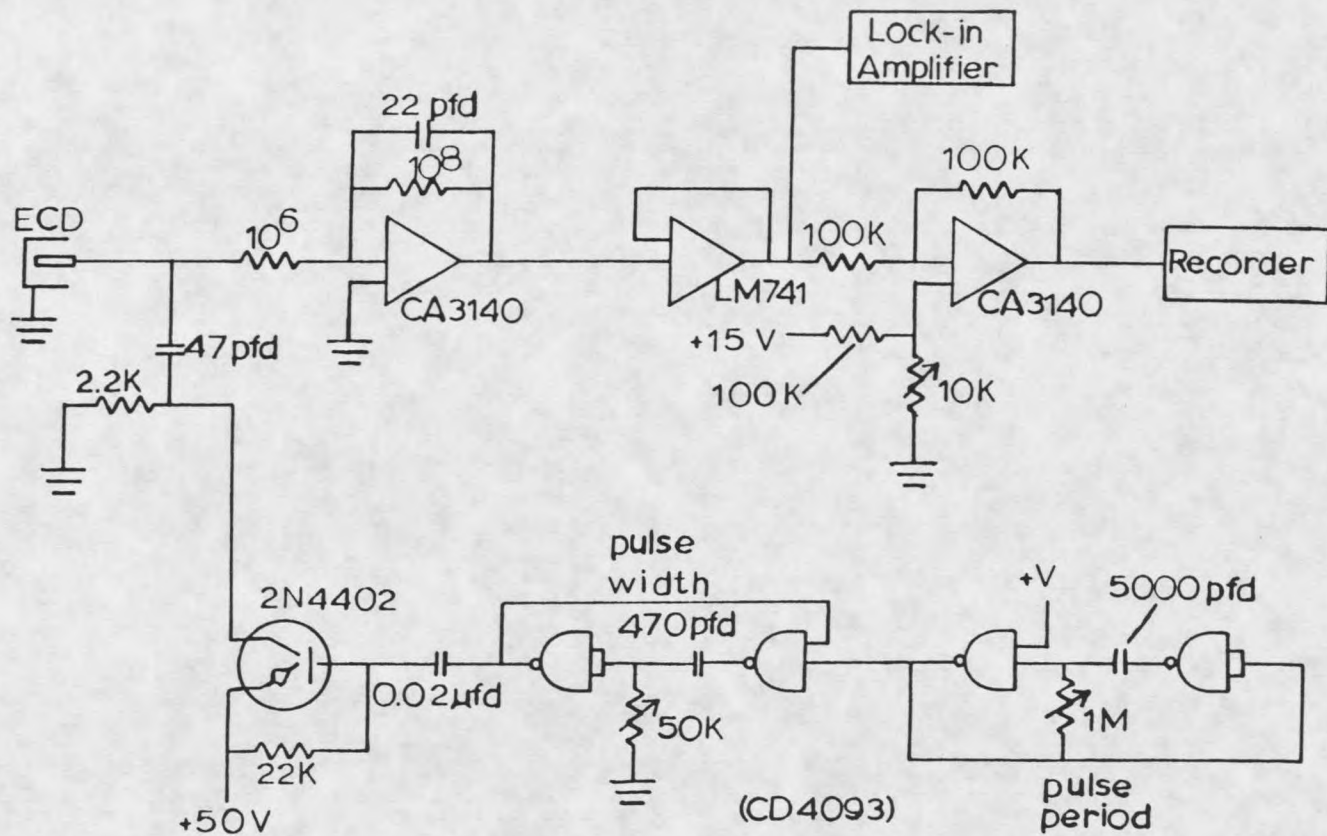


Figure 5. Circuit diagram for the pulser and electrometer used for the PDM-ECD .

in Figure 5. The fixed-frequency pulser was operated at 5 kHz. When Ar/CH₄ was used, the pulse width was set at 2 μs, while for N₂, the pulse width was 10 μs. After processing by the electrometer (48), the current signal from the ECD was sent to pen 1 of a two-pen chart recorder and to a lock-in amplifier (Princeton Applied Research, Model 5207), as shown in Figure 1.

The lock-in amplifier extracts and amplifies the modulated component of the ECD signal which has the same frequency as the reference signal from the chopper. For the quinone experiments involving electron capture enhancement, the phase angle offset was adjusted manually according to the chopping frequency. For all other experiments, the phase-angle offset was set at -26°, which was the optimal value for a chopping frequency of 23 Hz (18). The effect of the phase-angle offset on the output signal from the lock-in amplifier is important. Although the reference signal from the chopper and the modulated component of the ECD signal have the same frequency, the desired overlap of the two signals is very often not optimal. The phase angle offset control on the lock-in allows for adjustment of the temporal presentation of the reference signal to the mixer circuit of the lock-in. If the phase angle offset is adjusted so that the two signals are perfectly in phase, the output signal is a maximum.

(49). The modulated component of the ECD signal is sent from the lock-in amplifier to pen 2 of the recorder. Thus, pen 1 records the electron capture response, $\delta I_{L/C}$, within the PDM-ECD, while pen 2 simultaneously records the modulated response, δI_M , which results from photochemical processes occurring within the PDM-ECD.

Measurement of Photodetachment Spectra

Photodetachment spectra were obtained by repeatedly injecting the compound of interest while varying the wavelength of light in increments of 10 nm. The relative PD cross section, $\text{rel } \sigma$, was calculated by Equation 17 (18). The absolute photodetachment cross-section for

$$\text{rel } \sigma = \delta I_M / (\delta I_{L/C} \times \Phi) \quad (17)$$

iodide in the PDM-ECD was measured by Mock and Grimsrud (18). Calibration of the photodetachment spectra for the quinones was accomplished by including 1-iodooctane or 1-iodohexane in the sample (18).

Setup of the Atmospheric Pressure Ionization

Mass Spectrometer

An Atmospheric Pressure Ionization Mass Spectrometer (APIMS) was used for several of the experiments involving optically enhanced electron capture by quinone molecules. The basic design of the instrument has been described in considerable detail by Grimsrud and coworkers (8, 50-52).

However, a different data system was used and it was necessary to modify the ion source to allow the ionization region to be irradiated by the arc lamp. A schematic representation of the setup of the APIMS is shown in Figure 6.

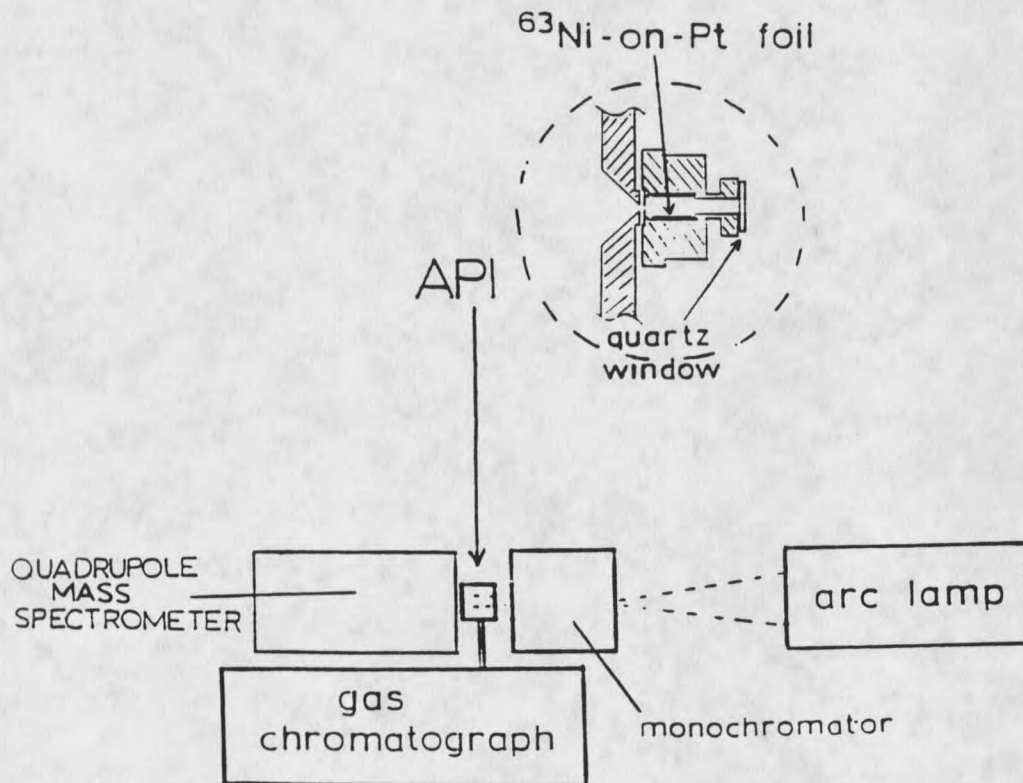


Figure 6. Apparatus used for APIMS studies.

Ion Source

The ion source was constructed from stainless steel with a 1.5 cm³ volume and a 15 mCi ⁶³Ni-on-Pt foil forming the cylindrical walls. It is comprised of two concentric cavities. The rear cavity, which is closest to the aperture, houses the ⁶³Ni foil and has a larger diameter than the front cavity. The front wall of the ion source was formed by a fused silica window, which was sealed by teflon washers and a metal faceplate. The circular hole in the faceplate was 0.71 cm in diameter, which was identical to that of the front cylindrical portion of the ion source block. The temperature in the source was maintained at 180°C, while the pressure in the source was 640 torr.

Optical System

The optical system was identical to that described previously for the PDM-ECD except that the optical chopper was not used. The lamp was positioned so that the light beam was on-axis with the cylindrical source and aperture, quadrupole rods and channeltron. The monochromator was positioned so that the entrance slit was at the focal point of the lamp. In one experiment, the monochromator was not used, and the full lamp power was allowed to enter the source as described previously.

Quadrupole

The quadrupole mass filter (Extranuclear Inc., Model 162-8) was operated at very low resolution. The ion extraction lens (lens 1) was operated at +24 V in order to minimize potential mass bias effects (52). Lenses 2-4 were operated at +24 V, 0 V and +24 V respectively. Instead of the strip chart recorder which had been in use previously with the instrument, a mass spectrometric data system (Vector One, Teknivent, Maryland Heights, MO) along with a Zenith 386-SX micro-computer was used to record and control the quadrupole mass filter.

Sample Introduction

The quinone samples were identical to those used in the PDM-ECD. They were introduced with a gas chromatograph (Gow-Mac, Bridgewater, NJ) to the ion source using the same column as was used in the PDM-ECD.

RESULTS AND DISCUSSION

Gas-Phase Photochemistry of Quinone Molecules
and Their Molecular Anions

The gas-phase interaction of *p*-benzoquinone (Q) with electrons and electron donors has been well studied (53-57). A particularly interesting characteristic of Q is that it attaches thermalized electrons extremely slowly (53, 56), despite its high electron affinity (1.9 eV).

Mock and Grimsrud (19, 20) used the PDM-ECD to study *p*-benzoquinone (Q), methyl-*p*-benzoquinone (MQ), 2,6-dimethyl-*p*-benzoquinone (DMQ) and tetramethyl-*p*-benzoquinone (TMQ). They showed that ultraviolet irradiation of the ionization volume caused an enhanced electron capture response for these compounds. The electronically excited triplet states of Q, MQ, DMQ, and TMQ were proposed to be responsible for this optical enhancement of electron capture (OEEC).

In ICR experiments, Brauman showed that the molecular anion of *p*-benzoquinone, Q^- , undergoes electron photodetachment in the UV-visible region of the spectrum (58, 59). Preliminary studies by Mock (44) indicated that the PDM-ECD could also be used to investigate PD of Q^- . However, both PD and OEEC occur simultaneously over a

portion of the UV spectrum. This greatly complicates the independent measurement of either PD or OEEC.

In this section, OEEC by quinone molecules and PD by quinone molecular anions will be further characterized and discussed. A method will be demonstrated which allows the study of either of these reactions without interference from the other. The PD spectra of the quinones will be shown and discussed. Finally, mass spectrometric measurements will be shown which suggest a possible mechanism for OEEC.

Description of the Problem

Figure 7 contains a series of chromatograms which show the effect of light on the electron capture response of Q. In each case, the concentration of Q was held constant while the wavelength of the incident light was varied. It can be seen from Figure 7 that with 240 nm light, the magnitude of the electron capture response to Q is significantly increased relative to the responses at 400 nm and without light. The light-induced response enhancement (RE) is calculated from the peak-height ECD responses with light of a specific wavelength, δI_λ and without light, δI_{NL} , according to equation 18:

$$RE = \delta I_\lambda / \delta I_{NL} \quad (18)$$

The enhancement of the ECD response is particularly large for Q, with $RE \approx 7$. The same OEEC is seen for the

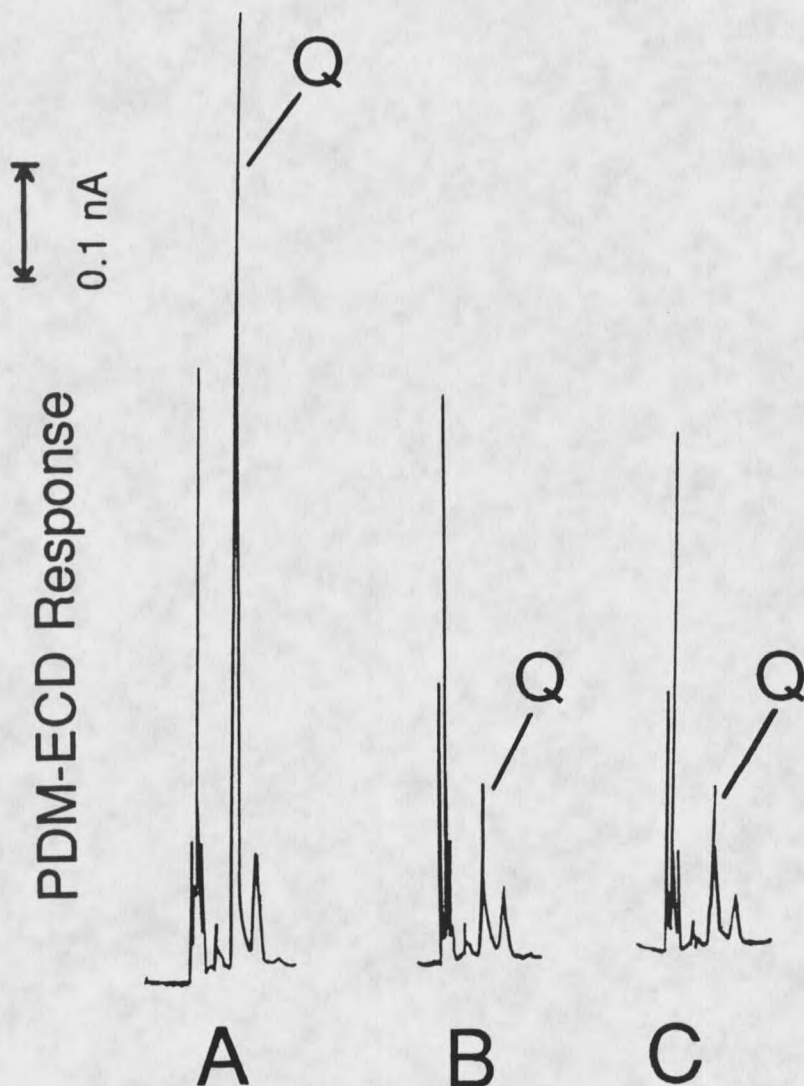


Figure 7.

Electron capture detector responses to 200 ng of *p*-benzoquinone through repeated GC analyses of a standard solution while varying the conditions of cell irradiation. Conditions are (A) monochromator set to 240 nm, (B) 400 nm and (C) light off. The ECD temperature is 180°C.

methylated derivatives of Q, although the RE values are not as great. OEEC responses were observed for the quinones between 210 and 320 nm, with maximum RE at about 240 nm. Q and its methylated derivatives undergo a photochemical process shown as Reactions 19a and 19b, in



which irradiation of the ionization volume results in a product which responds very strongly in the ECD.

Irradiation by ultraviolet light causes a significant decrease in electron density within the cell due to OEEC. However, in addition, Q and its methylated derivatives undergo electron photodetachment (PD), reaction 20, over



most of the same wavelength range. In contrast to OEEC, PD causes an increase in electron density within the cell during irradiation. The simultaneity of the two processes and their opposing effects on electron density within the cell make independent measurement of either process very difficult.

Characterization of OEEC

Using the PDM-ECD

In order to accurately measure the PD response of the quinone anions at short wavelengths without interference from OEEC, it is necessary to more fully understand the

nature of the OEEC response. In addition, it is of interest to discover the mechanism responsible for Reaction Sequence 19. For this reason, a general characterization of the OEEC response was undertaken.

Temperature Dependence of EC Response. If the quinone molecules have a positive temperature dependence for electron capture, a trivial local heating effect could be responsible for the OEEC response (60). After light absorption, a gaseous molecule may undergo radiationless relaxation by collisions with other molecules in its immediate vicinity. These collisions can result in heating of the buffer gas in the volume adjacent to the absorbing molecule. This explanation is unsatisfactory for the following reasons. One is that Q exhibits an ECD response that is relatively independent of temperature. Figure 8 shows a series of chromatograms of Q made at three different temperatures with the arc lamp turned off. The normal ECD response to Q is observed to be invariant from 100° - 200°C. The second reason is that if heating occurs by the mechanism described above, the effect should be proportional to the product of the light power and the absorptivity of the sample at the wavelength used (60). Although the UV absorption spectra of the quinones (to be discussed in detail in a later section) have strong absorption bands at 240 or 250 nm with nearly identical

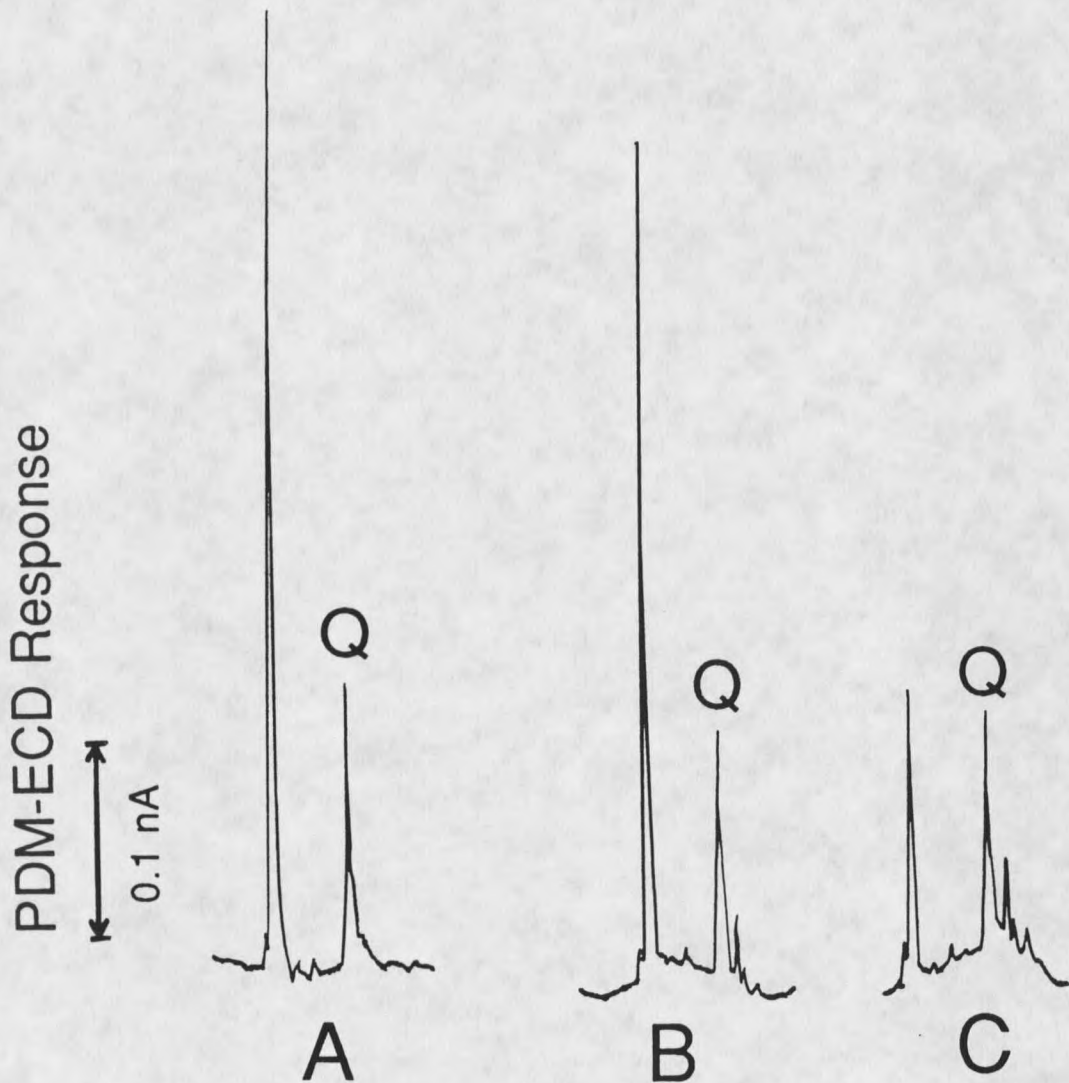


Figure 8.

Electron capture detector responses to 200 ng of *p*-benzoquinone through repeated GC analyses while varying the temperature of the cell without irradiation. Cell temperatures are (A) 100°C, (B) 150°C and (C) 200°C.

absorptivities (see Figure 16 on page 67) (61), the RE for Q at 240 nm is more than an order of magnitude greater than the RE for the other quinones at this wavelength (see Figure 15 on page 66). For these reasons, OEEC is not thought to be due to heating of the sample resulting from absorption.

Lack of OEEC for $C_{12}H_{26}$ and $C_{18}H_{38}$. The concentrations of the quinones within the ionization volume were relatively high, 10^{14} - 10^{15} molec cm^{-3} , while the EC rate constants for the quinones are known to be very low (20). It is therefore possible that OEEC results from a trivial physical perturbation of the cell caused by this combination of conditions. In order to determine whether this was the case, several long-chain hydrocarbons were introduced to the ECD at a high concentration in the presence of light. *n*-alkanes are known to exhibit extremely small EC responses (62). Injections of 3 μg (approximately 5×10^{14} molec cm^{-3} within the ionization volume) of dodecane and octadecane were made with the light turned off and with the full emission spectrum of the Xe lamp. For dodecane, very small EC responses were visible above the noise, but their magnitudes were the same with and without light. No response for octadecane was visible in either case.

Dependence of OEEC on Concentration. Figure 9 shows the concentration dependence of the EC response for Q with 240 nm light and without light. The EC response without light, δI_{NL} , is quite small and is observed to increase linearly with increasing concentration. Compounds that respond weakly in the ECD, such as Q, are known to exhibit linear responses with concentration because over most of the concentration range, a large population of electrons consumes only a small fraction of the analyte (63).

In contrast, the overall relationship between the measured response with light, δI_{240nm} , and Q concentration is nonlinear. The shape of the curve for δI_{240nm} vs. concentration bears considerable resemblance to the expected response curve for a strongly responding compound in the ECD (64). If the compound produced by the photochemical reaction in 19a is present at a sufficiently low concentration and its EC rate constant is large, a significant fraction of the compound is consumed by the electron capture reaction shown in 19b. Under these conditions, a linear response is expected (64). Examination of Figure 9 reveals that the response curve is approximately linear below about 500 ng. However, as the concentration of the compound is increased above 500 ng, the response curve is observed to be nonlinear. Under these conditions of increasing concentration, the

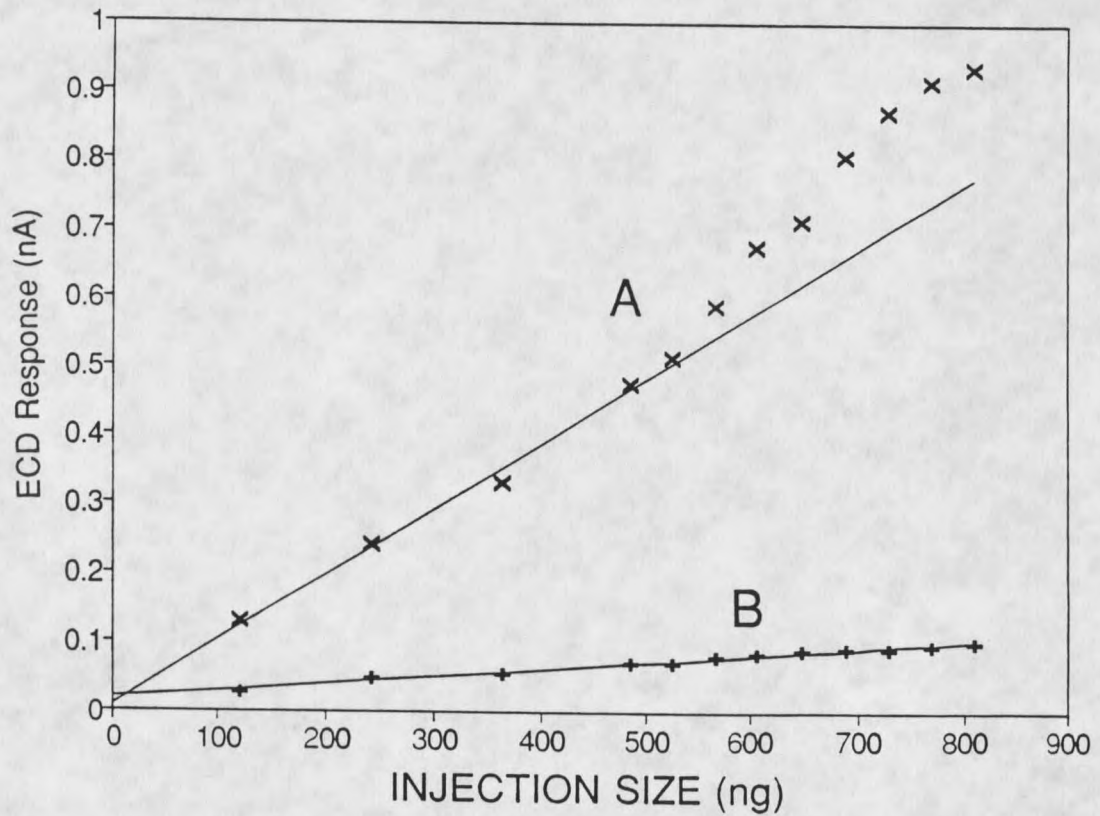


Figure 9. ECD response at varying concentrations of *p*-benzoquinone. In (A), the cell is irradiated with 240 nm light, while in (B), the cell is dark.

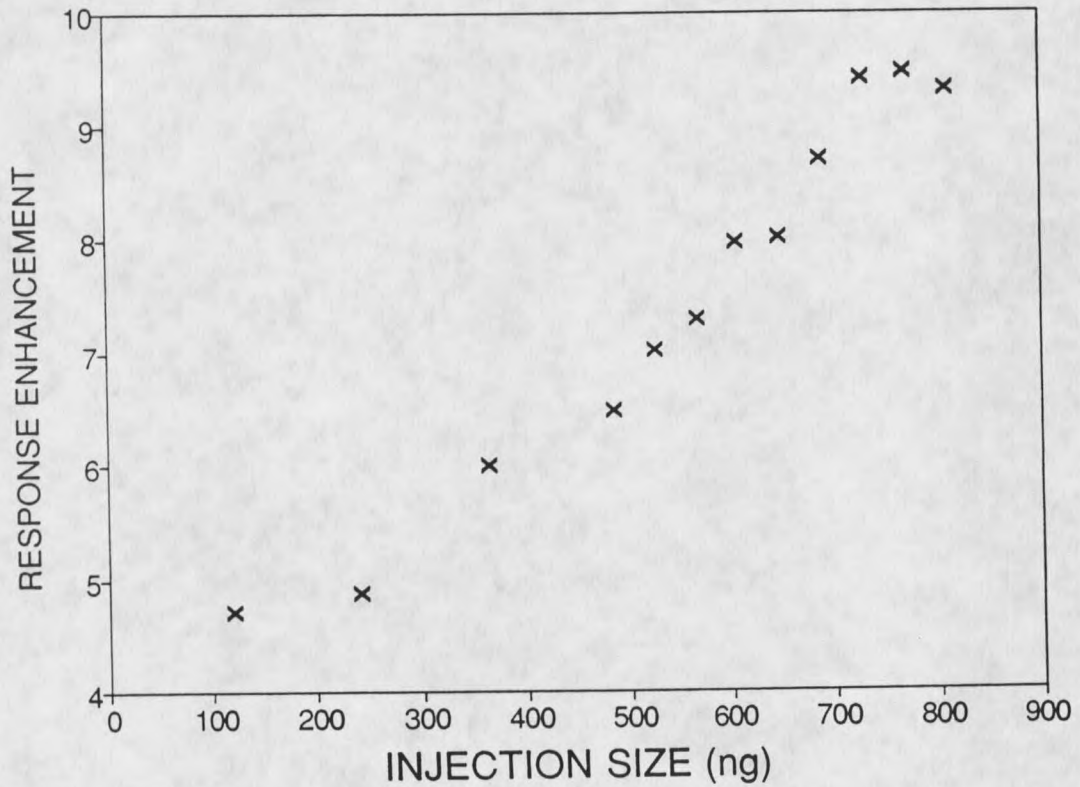


Figure 10.

Response enhancement (RE) of the PDM-ECD observed with light of 240 nm and at varying concentrations of *p*-benzoquinone. RE is the ratio of ECD response with light of a specific wavelength to the response without light. The values are calculated from Equation 5.

electrons react with a successively smaller fraction of Q and no longer alter its concentration as it passes through the cell. This results in the observed S-shaped response curve.

The RE values for each concentration were calculated from Figure 9 and are shown in Figure 10. The RE values are observed to increase steadily with concentration and are seen to resemble the concentration dependence of the $\delta I_{240\text{nm}}$ response in Figure 9.

Characterization of OEEC Using a Chopped Light Beam.

The OEEC response results from a large decrease in electron density within the cell during irradiation. It should therefore be possible to chop the light beam and examine the resulting modulation of the ECD signal. The modulated signal can be monitored by either of the following methods. Since the difference between the $\delta I_{240\text{nm}}$ and δI_{NL} responses is so large, the light beam can be chopped very slowly and the response observed as a measurable modulation superimposed on the normal EC chromatogram. A modulated signal can also be generated by chopping the light beam at a higher frequency. The resulting signal can then be processed in the same way as the PD-modulated signal, using the lock-in amplifier to extract the modulated component of the ECD signal and send the resulting output to pen 2 of the 2 pen chart recorder.

An experiment was performed during the elution of Q in which the speed of the recorder chart paper was increased to 1 cm/sec and the light beam was chopped at 0.5 Hz. The resulting EC chromatogram is shown in Figure 11. For comparison, the magnitudes of the normal $\delta I_{240\text{nm}}$ and δI_{NL} responses (measured without chopping) are also indicated. It is apparent from the chromatogram that upon blocking the light beam, the measured response decreases slowly over time. In addition, the difference between the "light on" and "light off" responses at the peak maximum of the modulated chromatogram is 0.74 nA, while the difference in the $\delta I_{240\text{nm}}$ and δI_{NL} responses is much larger, 1.31 nA.

To ensure that the above observations were not due to the speed of the recorder pen, the response characteristics of the chart recorder were measured. With chart recorder settings identical to those used above, the response of the pen was approximately 900 mV sec^{-1} , which is equivalent to 9 nA sec^{-1} . Since the pen responds significantly faster than the observed modulation, the above observations do not result from a slow recorder.

In a previous report, OECC was attributed to increased EC reactivity of quinone molecules excited into their triplet states (19). However, the triplet state of Q has a lifetime of $28.4 \mu\text{sec}$ against nonradiative

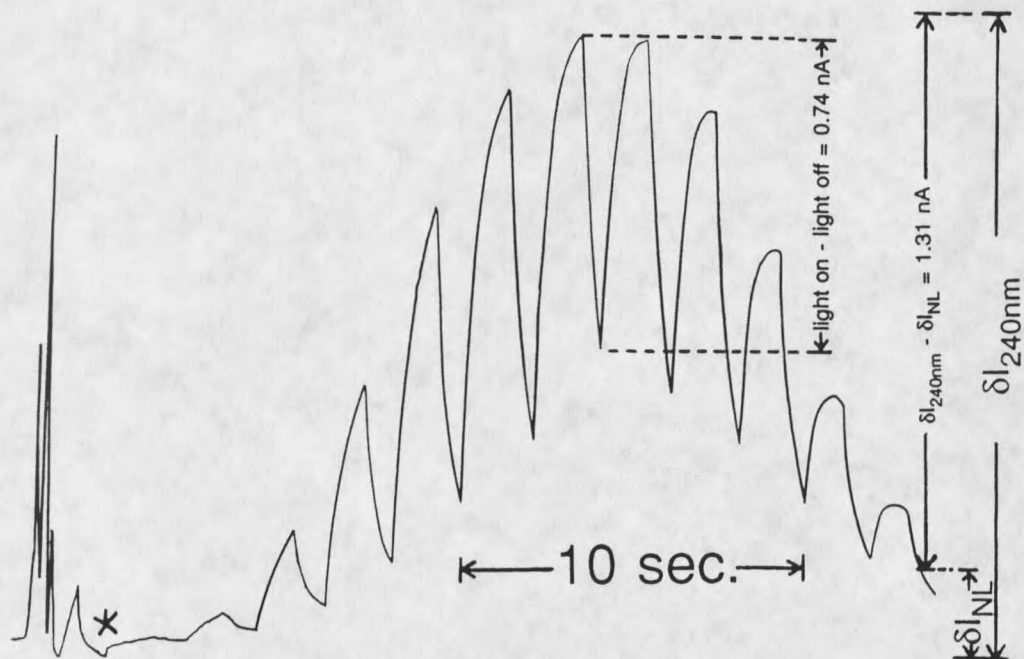


Figure 11.

GC analysis of *p*-benzoquinone during irradiation with 240 nm light. During the elution of *p*-benzoquinone, the chart paper speed was increased to 1 cm/sec and the light beam was chopped at 0.5 Hz. In the area of the chromatogram preceding the asterisk (*), the chart paper speed was 0.5 cm/min. The magnitude of the ECD response during irradiation with 240 nm light without chopping ($\delta I_{240\text{nm}}$) is also shown, along with the magnitude of the response without light (δI_{NL}).

relaxation to its ground electronic state (65). The triplet state of Q, ${}^3Q^*$, is not long-lived enough to account for the slow decay of the signal observed in Figure 11 when the light is extinguished. If ${}^3Q^*$ were responsible for OEEC, upon blocking the light beam, the recorded signal in Figure 11 would have been expected to decrease at the fastest rate allowable by the chart recorder. Instead, Figure 11 suggests a process with a slower time dependence than that for the radiationless deactivation of ${}^3Q^*$.

One simple process with a slow time dependence in the ECD is ventilation of the EC-active species from the cell. In order to more fully characterize OEEC and to determine if the above responses were due to cell ventilation, several chromatograms were recorded at different flow rates and chopping frequencies. It is helpful to interpret the data in the following manner used by Mock and Grimsrud (18). As discussed above, the difference between the "light on" and "light off" response at the peak maximum for the modulated chromatogram in Figure 11 is much smaller than the difference between non-modulated responses, $\delta I_{240\text{nm}}$ and δI_{NL} . α is the fractional decrease of the difference between these "light on" and "light off" responses with and without chopping. For example, from Figure 11, $\alpha = 0.74 / 1.31$, which leads to $\alpha = 0.56$. The

value for α is expected to decrease with increasing chopping frequency, according to Equation 21, where f is

$$\alpha = (1 + (2\pi f\tau)^2)^{-\frac{1}{2}} \quad (21)$$

the chopping frequency and τ is the time constant for the rate of change of the chemical system within the ECD (18). Equation 21 can be rearranged to the linear form shown in Equation 22, which can be used to determine τ if α and f

$$\zeta = (1/\alpha^2 - 1)^{\frac{1}{2}} = 2\pi f\tau \quad (22)$$

are known variables.

Chromatograms like the one in Figure 11 were recorded at buffer gas flow rates of 56, 77 and 115 mL/min with chopping frequencies between 0.4 and 2 Hz. As the chopping frequency was increased at a given flow rate, the visible modulation on the EC chromatogram decreased dramatically. Values for α were calculated at each chopping frequency and were also observed to decrease with increasing f as expected. The data is graphed in Figure 12 according to Equation 22. Values for τ at each buffer gas flow rate were determined from the plot and are also shown. Two important observations can be made from the graph. First, the values for τ are about four orders of magnitude greater than the lifetime of $^3\text{O}^*$. Second, these relatively large values for τ decrease sharply with increasing gas flow through the cell. The large τ values indicate that $^3\text{O}^*$ is not responsible for OEEC and they

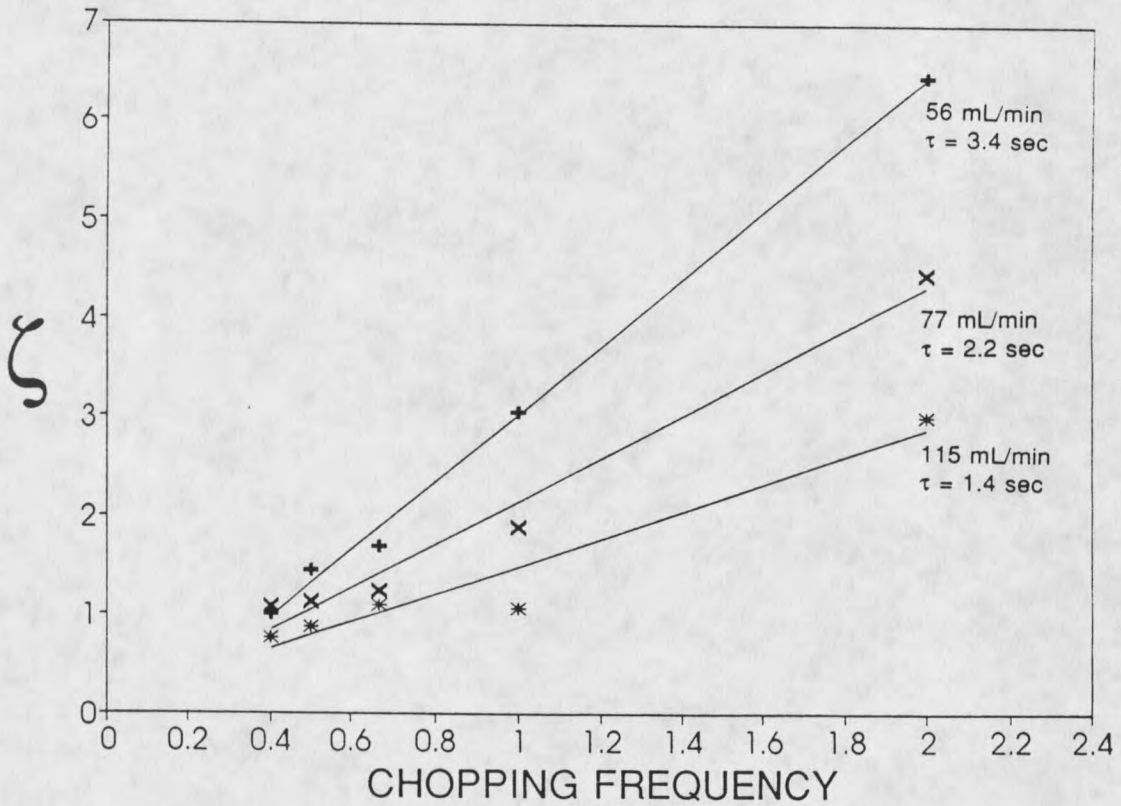


Figure 12.

Graph of Equation 9 used to calculate the time constant (τ) for the rate of change of the chemical system within the ECD at three different flow rates. τ for each flow rate is indicated on the graph. ζ is a function of the difference between the light-on and light-off responses of the PDM-ECD and is proportional to the chopping frequency. The straight lines are the least-squares fits of the points that were used to determine τ for each flow rate.

strongly suggest that the EC-active species produced by Reaction 19a is a stable molecule. The slow decrease in the enhanced EC response when the light is extinguished is simply due to ventilation of this stable photoproduct from the cell.

The modulation on the EC chromatograms was quite large in the previous experiments with slow chopping frequency. It should therefore be possible to monitor the OEEC response with the lock-in amplifier. As stated in the Experimental section, the lock-in extracts the modulated component of the ECD signal which has the same frequency as the chopper and sends the resulting processed signal, δI_M , to pen 2 of a two pen chart recorder. The output from the lock-in depends not only on the amplitude of the signal modulation, but also on the time lag between the reference square wave and the modulation of the EC signal. To maximize the output of the lock-in, the phase angle offset, θ , is adjusted. When Q is present, the electron density in the cell decreases when the light is on and increases when the light is off. Therefore, a negative signal from the lock-in is expected when θ is optimized for maximum output.

Using the lock-in to process the modulated signal in the manner described above, several experiments were performed with Q. As f was varied from 5 to 43 Hz, the

necessary θ for the maximum negative response from the lock-in was found to be -90° in all cases. The OEEC-modulated response, δI_M , was eliminated at all chopping frequencies when θ was adjusted to 0° . Previously, it was stated that the visible modulation of the EC response decreased dramatically when f was increased from 0.4 to 2 Hz. The OEEC-modulated response follows this trend at higher chopping frequencies, as it decreases steadily from 5 to 43 Hz and is completely eliminated at $f = 53\text{Hz}$.

The previous observations are explained with the aid of a drawing adapted from reference 18 and shown in Figure 13. This drawing shows the two waveforms that are sent to the lock-in. The chopper produces the square wave, while the ECD signal is represented by the other waveform. This illustration depicts the use of successively faster chopping of the light beam from Figures 13A to D. When the two signals are exactly 180° out of phase, as shown, the processed signal from the lock-in reaches its maximum negative value. At the top of the figure is shown the phase angle offset necessary to orient the waveforms so that they are 180° out of phase. The shaded area under the waveforms indicates the magnitude of the lock-in output, δI_M , for each case. In Figure 13A, f is slow with respect to the attainment of a stable light-on and light-off ECD signal, and the necessary θ is near 0° . However,

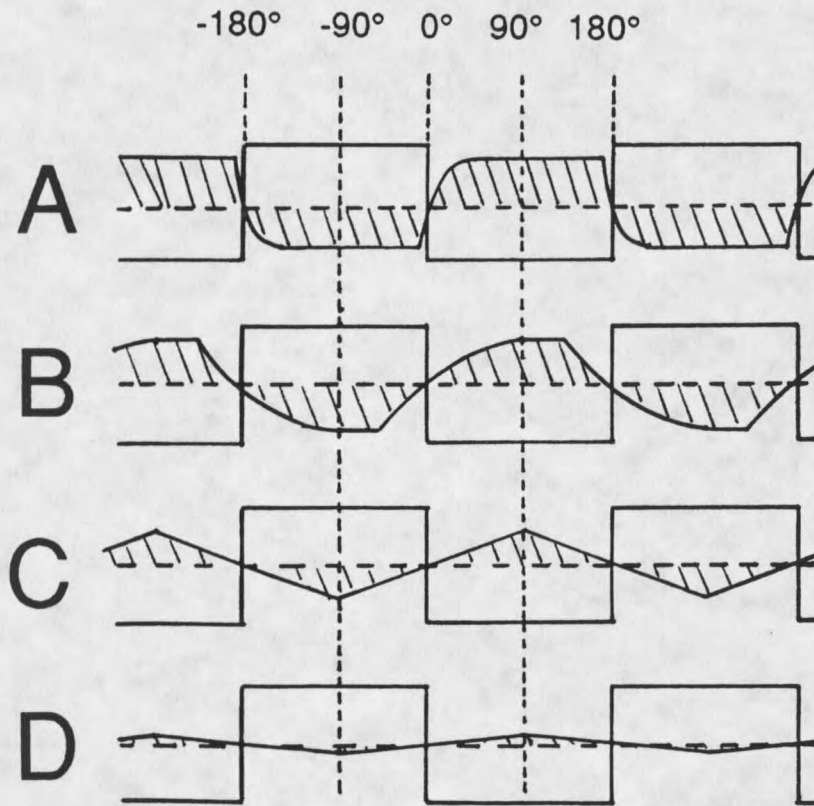


Figure 13. Simulations of the two waveforms sent to the lock-in amplifier. The phase angle offset necessary to achieve the maximum negative output from the lock-in is shown at the top. The light beam chopper produces a square wave, the frequency of which increases from A to D. The other waveform is the ECD signal received from the electrometer.

with increasing f , the modulation of the ECD signal is expected to lag increasingly far behind the light pulses until the situation in 14C is reached. In this case, the modulation assumes the shape of a triangular wave because the time between light pulses is much shorter than the time necessary for the ECD signal to stabilize. For these conditions, a value for θ of -90° is necessary to properly orient the two signals so they are 180° out of phase. A further increase in f still results in a triangular wave, but with smaller amplitude, as in 14D. The proper θ value remains at -90° . At any chopping frequency, if θ is adjusted so that the two signals are exactly 90° out of phase, the output from the lock-in will be zero. This occurs because the in-phase overlap and the out-of-phase overlap of the two signals are equal, which results in a cancellation of the lock-in signal.

The above explanation is consistent with the experimental observations of decreasing OEEC-modulated response with increasing f and a phase angle offset of -90° in all cases. It also explains the experimental observation that the OEEC-modulated response disappeared when θ was set to 0° .

Method For Independent Measurement of OEEC and PD.

It was previously stated that measurement of PD and OEEC for quinone molecules is difficult because both processes

occur over the same wavelength range and have opposite effects on the electron density within the cell. The above discussion of lock-in responses to OEEC suggests a method for independent measurement of OEEC and PD. However, it is first necessary to review several aspects of the photodetachment response of the PDM-ECD.

Mock and Grimsrud investigated many experimental parameters related to the PD-modulated response, including chopping frequency and phase angle offset (18). They discovered that for the PD-modulated response, θ decreased from -90° to a value near 0° as f decreased from 73 Hz to 13 Hz. To further investigate the lock-in response due to PD, Q^- and 1-iodohexane were introduced into the ECD while the cell was irradiated with 315 nm light. I^- is produced from 1-iodohexane by dissociative EC. The relationship between θ and f was studied and the responses were compared. Q^- and I^- exhibited identical dependencies of θ on f for the PD-modulated response. At $f = 5$ Hz, the PD-modulated response was maximized at $\theta = 0^\circ$ and was completely eliminated at $\theta = -90^\circ$. In contrast to the OEEC-modulated response, the PD-modulated response is moderately fast on the time scale established by the chopping frequency of 5 Hz (18). At this value of f , the ECD signal waveform due to PD is thought to resemble a square wave as shown in Figure 13A. Therefore, the

necessary value for θ is 0° in order to maximize the PD-modulated response. When θ is changed to -90° , the lock-in output is eliminated because the in-phase overlap and the out-of-phase overlap are equal and cancel each other out.

As stated previously, at a chopping frequency of 5 Hz, the OEEC-modulated response disappears at $\theta = 0^\circ$, where the PD-modulated response is maximized. With $\theta = -90^\circ$, the reverse is true. Therefore, although both PD and OEEC may occur simultaneously over a portion of the ultraviolet spectrum, the contribution to the modulated response at pen 2 by either process can be selectively eliminated. This allows for independent measurement of either PD or OEEC without interference from the other.

PD Spectra of the Quinone Molecular Anions

In this section, the PD spectra of the molecular anions of Q, MQ, DMQ, and TMQ will be shown and discussed. These spectra were obtained at 180°C with a chopping frequency of 5 Hz and a phase angle offset of 0° . All other important parameters are listed in Experimental. The spectra are shown in Figure 14. In Figure 14A, in addition to the PD spectrum for Q^- , the known condensed phase absorption spectrum of Q^- is shown (66). The PD spectra of the quinone anions are qualitatively analogous to those of the nitroaromatic anions measured by Mock and

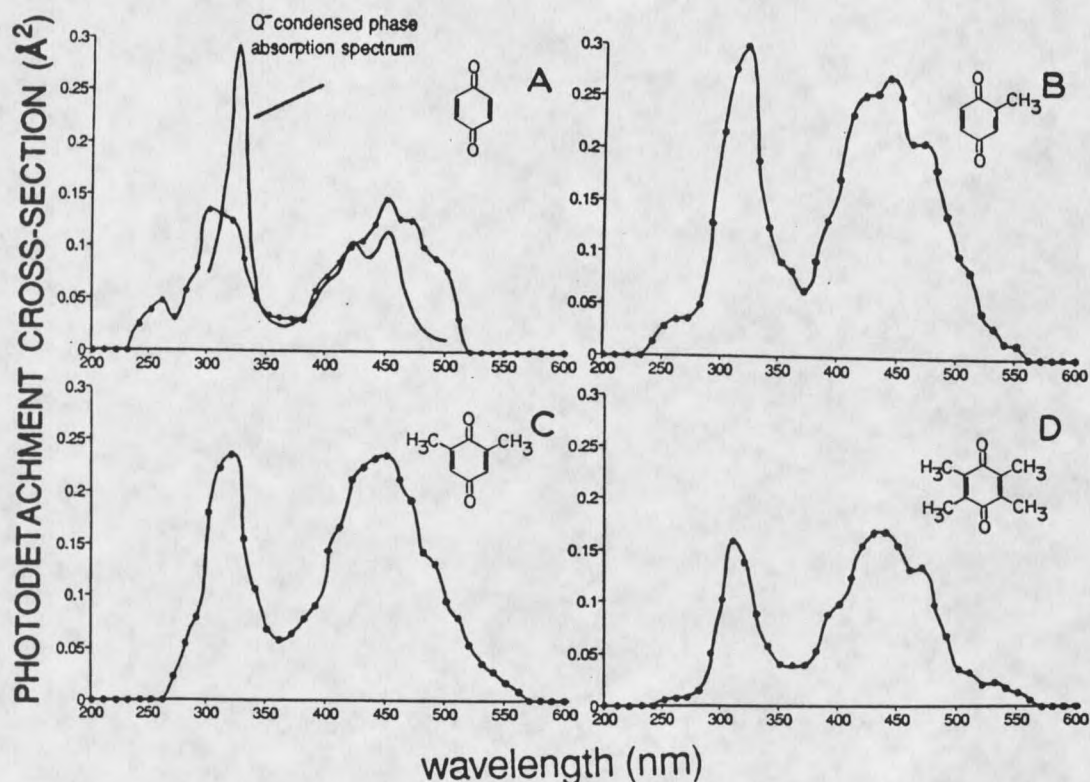


Figure 14.

Electron photodetachment spectra of the quinone molecular anions. These spectra were measured by the PDM-ECD at 180°C. A chopping frequency of 5 Hz was used along with a phase angle offset of 0° to ensure there would be no interference from OEEC. Absolute PD cross-sections were determined by comparison with the PD measurements of I^- at 365 nm. Measurements were made at 10 nm intervals. In (A), the condensed phase absorption spectrum is shown for the molecular anion of *p*-benzoquinone (66). The absorption spectrum was measured in an optically transparent thin layer electrode cell.

Grimsrud (10), so they will be interpreted in a similar manner. The PD spectra of the quinone anions have two general important characteristics. First, the spectra of the four anions all exhibit a PD threshold in the 510 - 560 nm range. Second, the spectra exhibit two maxima at about 450 nm and 310 nm. It is thought that direct photodetachment is responsible for PD in the threshold region of the spectra, whereas peaks and maxima in the spectra are due to resonance photodetachment.

Direct Photodetachment. The threshold for direct photodetachment from an anion often occurs in a wavelength range where the photon energy is close to the electron affinity (EA) of the neutral (10). The EA corresponds to the 0-0 transition from the anion to the neutral, and the threshold for direct PD is usually observed at an energy equal to the vertical transition between the anion and the neutral (23). If the geometries of these two species differ significantly, the neutral will be formed in one of the higher vibrational or rotational energy levels of its electronic ground state (10). In this case, poor Franck-Condon overlap exists and the threshold energy for direct PD is expected to be greater than the EA.

Table 1 compares E_{th} , the minimum photon energy at which PD is observed, with the EA for each of the quinones which was determined by PHPMS (67). The threshold

wavelength, λ_{th} , from which E_{th} was calculated is also shown. The uncertainty in λ_{th} is ± 20 nm and results from the bandwidth of the monochromator. At wavelengths of 510 - 560 nm, this converts to an uncertainty in E_{th} of ± 0.1 eV. Included in Table 1 are reported values for the entropy of negative ionization, ΔS° , for Q and MQ (55).

From the comparisons in Table 1, it is observed that the experimentally measured values of E_{th} for the quinones occur at a photon energy 0.4 - 0.6 eV above the EA.

Table 1.

Photodetachment thresholds of the quinone anions.

Anion	PDM-ECD ^a		PHPMS ^d	
	λ_{th} (nm) ^b	E_{th} (eV) ^c	EA (eV) ^e	ΔS° (eu) ^f
Q	510	2.43	1.91	-4.0
MQ	550	2.26	1.85	-4.0
DMQ	560	2.21	1.78	
TMQ	560	2.21	1.59	

^a Present work, from Figure 14.

^b Highest wavelength setting of monochromator at which PD is observed. Uncertainty is ± 20 nm.

^c Photon energy corresponding to λ_{th} . Uncertainty is ± 0.1 eV.

^d PHPMS measurements from reference 67.

^e Electron affinity. Uncertainty is ± 0.1 eV.

^f Entropy change associated with negative ionization of molecule, $M \rightarrow M^-$.

In preliminary PDM-ECD studies of Q (44), Mock also reported a value for E_{th} that was approximately 0.4 eV above the EA. He interpreted this result as an indication that there exists a relatively large difference in geometry between the anion and the neutral. This conclusion was based on the large decrease in entropy (-4.0 eu) reported by Chowdhury et al. (55) for the formation of Q^- from Q. It is thought that the above explanation accounts for the difference between E_{th} and EA for MQ, DMQ and TMQ as well.

In two reports (58, 59), Brauman et al. utilized an ion cyclotron resonance mass spectrometer (ICR) to obtain the high and low resolution PD spectra of Q. The high resolution laser PD spectrum (58) only includes data from 700 - 580 nm and shows $\lambda_{th} = 610$ nm, which converts to 2.03 eV. This value is in fairly good agreement with the EA value determined by Kebarle et al., but not with the results of the PDM-ECD. The low resolution PD spectrum (59) was measured from 700 - 260 nm. The light source was a 1000 W arc lamp used with a monochromator to give a bandwidth of 5 - 24 nm (the exact bandwidth of light was not specified). In this report, the PD onset was given as 610 - 615 nm although the actual PD spectrum from the paper shows an apparent onset for PD at about $\lambda_{th} \approx 520$ nm.

Either of two factors could possibly contribute to the discrepancy between the two ICR measurements and between the ICR and PDM-ECD measurements of λ_{th} . First, the high-power laser light probably gives much greater sensitivity than an arc lamp for detection of the PD signal. This could account for the difference in the apparent λ_{th} measurements between the two ICR reports. It could also entirely account for the difference between the PDM-ECD and ICR measurements. Second, because of the low pressure within the ICR cell (10^{-8} - 10^{-5} torr), infrequent collisions result in ions with greater-than-thermal energies (23). This problem is compounded because Q^- was produced in the ICR experiment by electron capture, a process that produces anions with high internal energies. A small PD cross section was visible at wavelengths longer than λ_{th} in the high resolution laser PD spectrum and was attributed to PD from vibrationally excited anions. It is conceivable that these "hot bands" could also be responsible for PD at shorter wavelengths than λ_{th} . It is not known whether this explanation can account for the 100 nm difference in λ_{th} between the laser ICR measurement and the PDM-ECD measurement.

Resonance Photodetachment. The two peaks observed in the PD spectra of the four quinone anions are thought to be due to resonance PD. At wavelengths where resonance PD

occurs, interaction of a photon with the anion of interest does not cause direct electron detachment from the ion. Instead, the anion first absorbs the photon of light to form the excited negative ion. The electronically excited anion can relax back to the ground state, or undergo autodetachment to form the corresponding neutral and a free electron (10). Resonance PD is the process of photon absorption by the anion followed by autodetachment of an electron.

Since the process of resonance PD is initiated when the anion absorbs a photon, the peaks present in the PD spectrum should also be present in the absorption spectrum of the anion. The UV-visible absorption spectrum of the *p*-benzoquinone anion was reported by Gamage, Umapathy and McQuillan (66). They generated Q^- by reduction of Q in DMSO at -1.0 V in an optically transparent thin layer electrode cell. The spectrum was recorded by a commercial UV-visible spectrometer and is shown in Figure 14A. In order to make comparisons with the PD spectra, molar absorptivity was converted to cross section.

A qualitative comparison of the absorption and PD spectra reveals that they are indeed very similar. The two maxima in the absorption spectrum at 451 and 424 nm are matched by a peak at 450 nm in the PD spectrum. The strong absorption at 325 nm coincides with a smaller,

broader peak in the PD spectrum. In a previous comparison of the condensed phase absorption spectrum with the PD spectrum for the nitrobenzene anion (10), the short wavelength absorption peak was also observed to have a larger cross section than the corresponding PD resonance. It is not known whether this phenomenon is an indication of the efficiency for autodetachment versus relaxation from the excited *p*-benzoquinone anion or simply a manifestation of the extreme difference in physical conditions between the gas phase and condensed phase experiments. Unfortunately, the absorption spectra for the methylated quinone anions are not available.

Intercomparison of the PD spectra of Q, MQ, DMQ and TMQ, reveal that their shapes are quite similar. The two resonances are present in all four spectra in the same spectral regions. It is observed that the PD cross sections for MQ and DMQ are much greater than those for Q and TMQ at the wavelengths where strong resonance PD occurs. This could be an indication that the absorption cross sections for MQ and DMQ are greater than for Q and TMQ. Alternatively, it could indicate that autodetachment is more efficient for MQ and DMQ than for Q and TMQ.

OEEC Spectra of the Quinones

In this section, the wavelength dependence of the OEEC response for the quinones will be discussed. The

OEEC spectra of Q, MQ, DMQ and TMQ will be reported and compared to their condensed-phase absorption spectra. The experiments were performed at 180°C with a chopping frequency of 5 Hz. The phase angle offset of the lock-in was set at -90° to obtain the maximum negative OEEC-modulated response, δI_M , and to eliminate any contribution from PD. The spectra were graphed in a form similar to the PD spectra. The relative OEEC cross section, $\text{rel } \sigma_{\text{OEEC}}$, was calculated at each wavelength from Equation 23

$$\text{rel } \sigma_{\text{OEEC}} = \delta I_M / (\delta I_{\text{NL}} \times \Phi) \quad (23)$$

(Φ is the relative photon flux at each wavelength at the exit slit of the monochromator).

The OEEC spectra of Q, MQ, DMQ and TMQ are shown in Figure 15. The OEEC cross section for Q at 240 nm is more than an order of magnitude larger than for its methylated derivatives. For this reason, the scale of the y-axis in Figure 15A is larger than for the other three spectra. All of the spectra exhibit a prominent peak. For Q, MQ and DMQ, the peak reaches a maximum at 240 nm, while for TMQ, the peak is at 250 nm. The spectra for MQ and DMQ each show a small additional peak at about 300 nm.

Figure 16 shows the condensed-phase absorption spectra of Q, MQ, DMQ, and TMQ reported by Braude (61). The maxima observed in Figure 15 are also seen in the absorption spectra at approximately the same wavelengths.

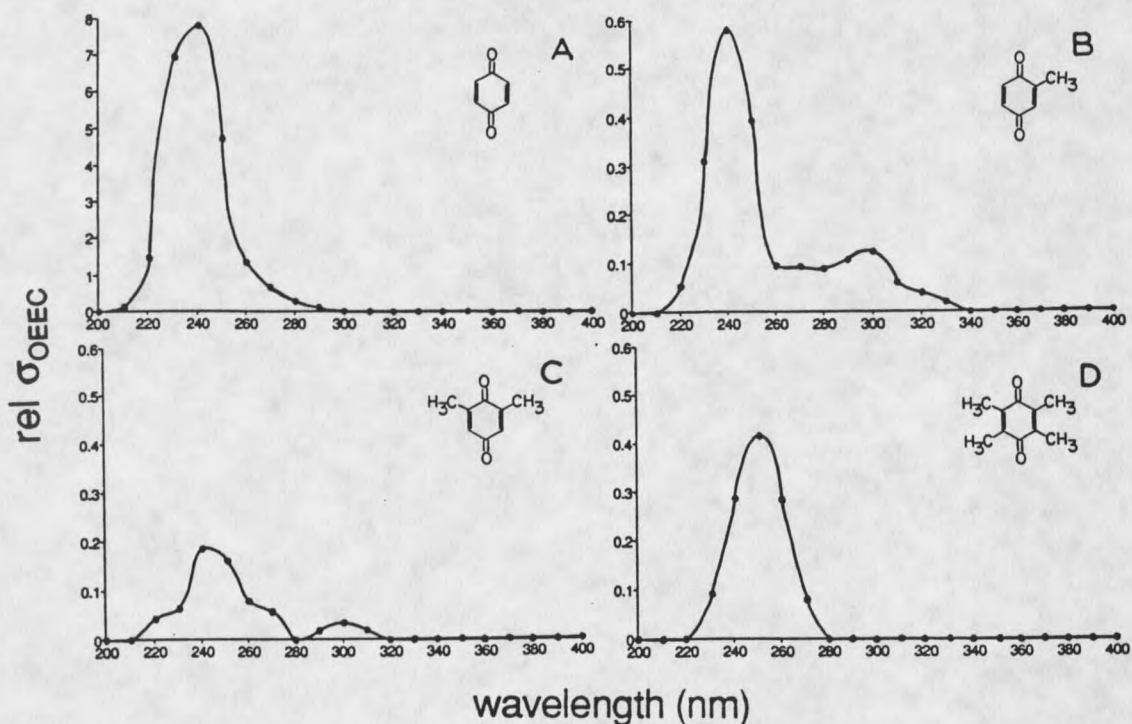


Figure 15.

OEEC spectra of the quinones measured by the PDM-ECD at 180°C. The $\text{rel } \sigma_{\text{QEEC}}$ is calculated from Equation 11 and is the ratio of the negative modulated response to the response without light and the light flux at the wavelength used. The spectra were recorded with a chopping frequency of 5 Hz and a phase angle offset of -90° to ensure that there would be no interference from PD.

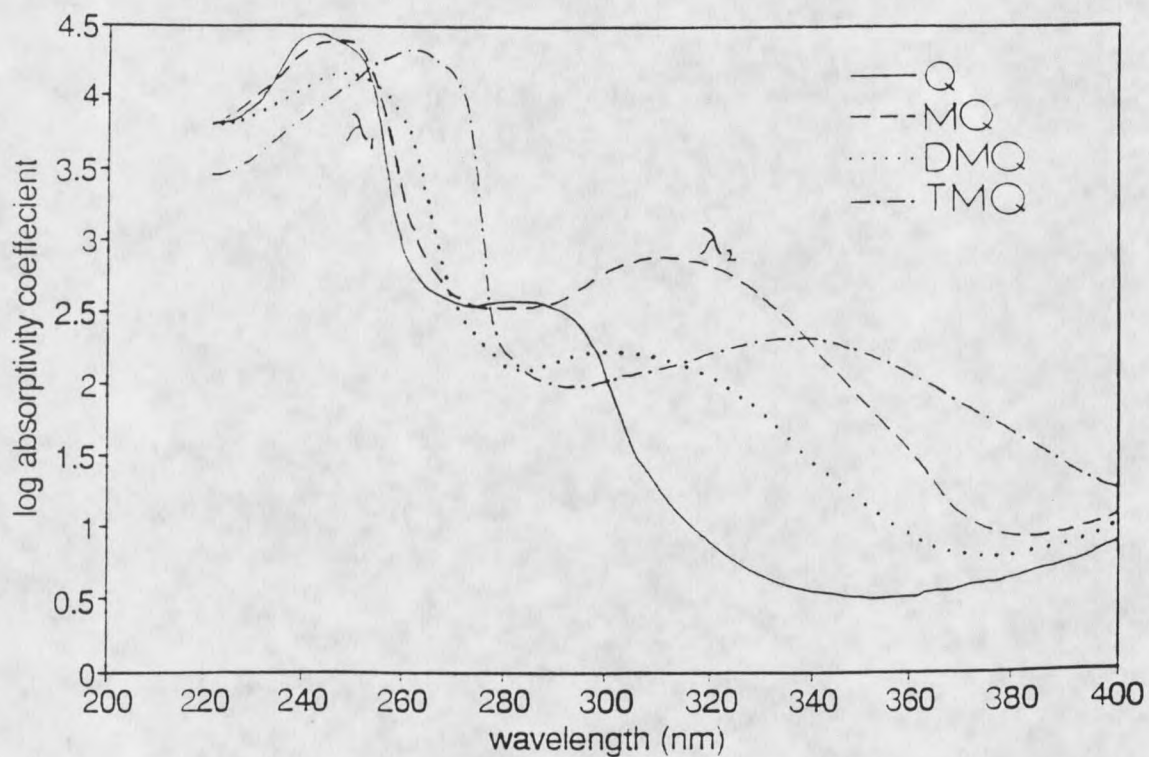


Figure 16. Absorption spectra in *n*-hexane of the quinones taken from Braude (61). Absorptivity coefficients are in units of $\text{dm}^3 \text{mol}^{-1} \text{cm}^{-1}$.

The absorption spectra of Q, MQ and DMQ show a strong absorption at 240 nm, which is also observed in the OEEC spectra (in Figure 16, the wavelength range where this strong absorption occurs is labeled λ_1). The same is true of the strong absorption at 250 nm for TMQ. In addition, the small peaks in the OEEC spectra of MQ and DMQ at 300 nm are observed as less intense absorption bands in the 300 nm region (λ_2) of Figure 16. The absorptions at λ_1 and λ_2 for the quinones are thought to be due to $\pi^* \leftarrow \pi$ transitions from the electronic ground state of the neutral quinone molecule to excited singlet states of the neutral (68). For the strong absorption in the λ_1 region, all of the quinones are seen to have nearly identical absorptivities. However, as it was noted above, the peak for Q at λ_1 is about ten times larger than those of MQ, DMQ and TMQ. The preceding observations lead to the following conclusion: although the process responsible for OEEC by quinone molecules includes electronic excitation of the neutrals, the magnitude of the OEEC response is significantly affected by other considerations.

Characterization of OEEC Using APIMS

In a previous section, it was suggested that the species responsible for OEEC and produced by Reaction 19a is a stable molecule. However, with the PDM-ECD, it was

not possible to determine the identity of this molecule. In order to identify the ions present in the ECD volume during irradiation, an atmospheric pressure ionization mass spectrometer (APIMS) was used. The ion source of the APIMS is described in detail in Experimental. It is similar to that of the PDM-ECD in that it is cylindrical and employs a ^{63}Ni foil to produce ionization. In comparison to the PDM-ECD, the ionization volume is slightly smaller, 1.5 cm^3 , and is comprised of two concentric cavities. The rear cavity, which is closest to the aperture, houses the ^{63}Ni foil and has a larger diameter than the front cavity. Although there are some small differences between the APIMS ion source and the PDM-ECD ion source, these differences are expected to be minimal and the internal conditions of the two cells are thought to be similar (10). Because the light beam was positioned on-axis with the cylindrical ion source and the channeltron detector, it was necessary to verify that the presence of photons did not alter the response of the channeltron. Without sample present in the source, it was determined that the total ion current and the mass spectra were virtually identical with the light on and with the light off.

After determining that the presence of light did not adversely affect the normal operation of the APIMS,

several experiments were performed in order to measure the mass spectra of Q during irradiation. As noted in Experimental, in order to obtain better signal intensities, a low resolution was used during the acquisition of the mass spectra.

The mass spectrum of Q obtained without light is shown in Figure 17A. It exhibits one significant peak at $m/z = 108$, which corresponds to the molecular ion, Q^- . Figure 17B shows the mass spectrum taken during irradiation with 240 nm light. It is observed that the magnitude of the Q^- peak at $m/z = 108$ is nearly identical to that of Figure 17A and that a large peak at $m/z = 216$ is also observed. Figure 18 shows the single ion chromatograms for masses 108 and 216 during the elution of Q from the column. The signal for $m/z = 216$ is seen to increase above the noise only after the peak for $m/z = 108$ has nearly reached its maximum. The signal for $m/z = 216$ is also observed to decrease rapidly long before the signal for $m/z = 108$ diminishes significantly.

In another experiment, the source was irradiated by 240 nm light until the TIC peak due to Q^- was near its maximum. At this point, the light was abruptly extinguished. The mass spectra were measured before and after turning off the light and are shown in Figure 19. The mass spectrum in Figure 19A was recorded immediately

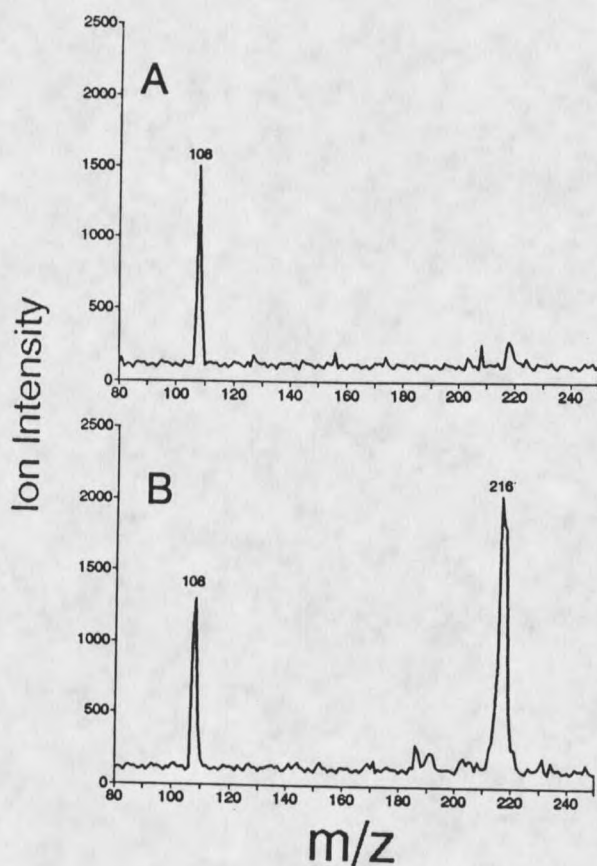


Figure 17.

Negative ion mass spectra of *p*-benzoquinone recorded on an atmospheric pressure ionization mass spectrometer at 180°C. In (A) the cell was not irradiated, while in (B) the ion source was irradiated with 240 nm light. A low resolution setting was used on the instrument in order to achieve better signal to noise.

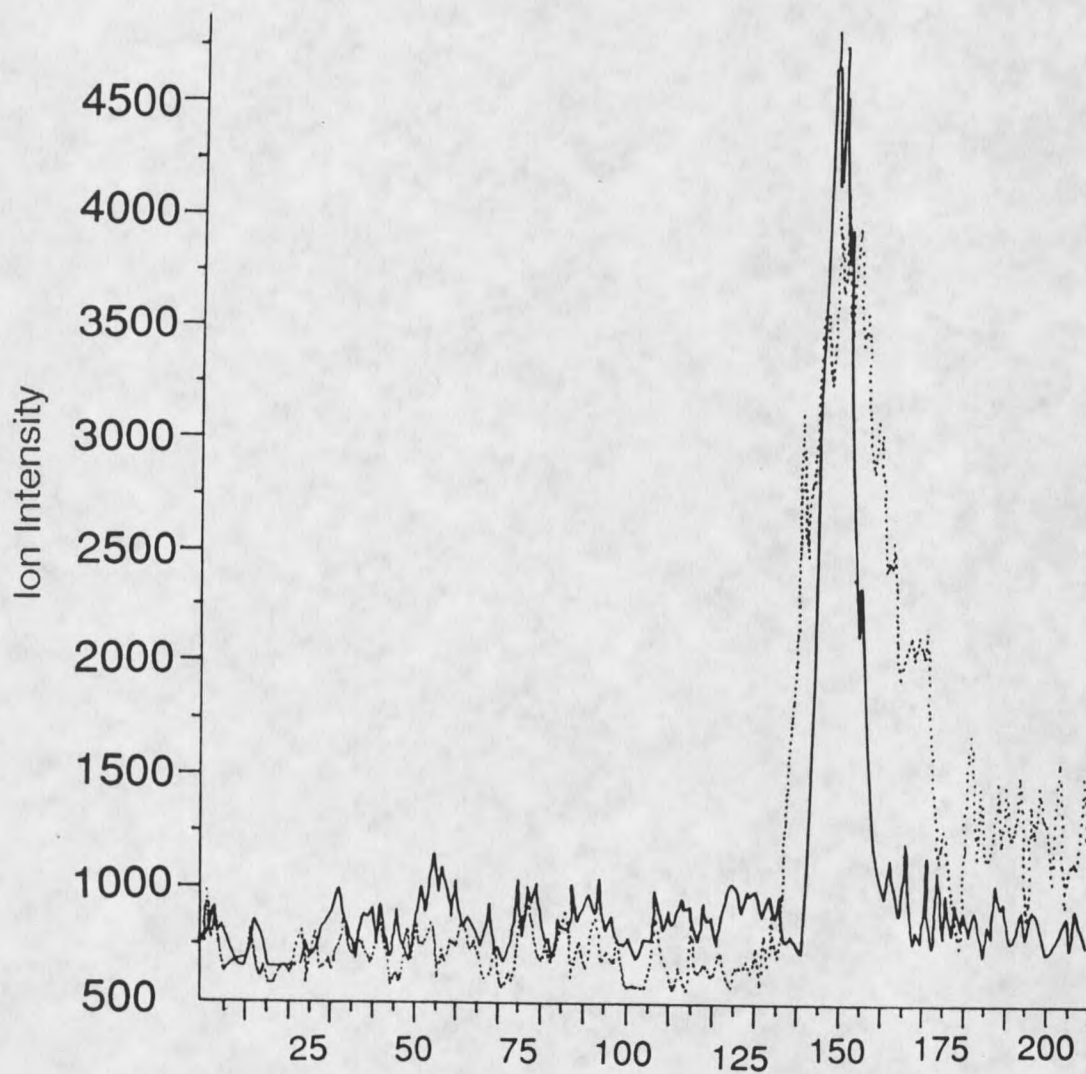


Figure 18. Superimposed single ion chromatograms from Figure 17. The sums of the masses that comprise the wide resolution envelope (5 amu wide) around $m/z = 108$ (dotted line) and $m/z = 216$ (solid line) were plotted as a function of time to give the chromatograms.

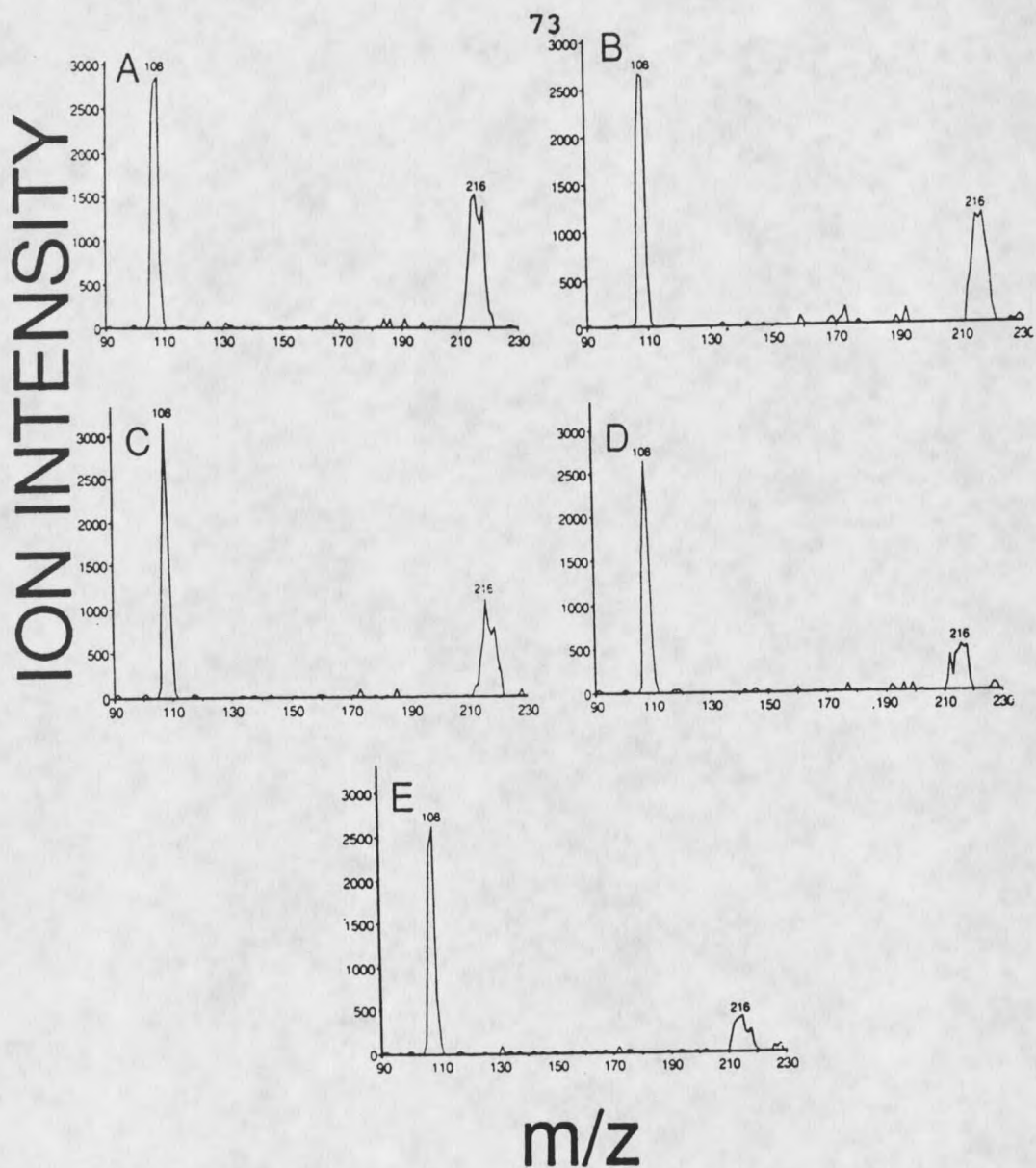


Figure 19.

Low resolution APIMS negative ion mass spectra of *p*-benzoquinone recorded before and after abruptly extinguishing the light. The spectra were processed by subtracting the background signal present prior to elution of Q from the column. The spectra were recorded as follows: (A) immediately prior to extinguishing the light, (B) 0.33 sec after extinguishing the light, (C) 1.0 sec after, (D) 1.67 sec after and (E) 2.33 sec after.

prior to extinguishing the light. The mass spectra shown in Figure 19B-E were taken at successively longer intervals after extinguishing the light. In these five spectra, the peak at $m/z = 108$ is observed to be relatively invariant. However, the peak at $m/z = 216$ is seen to slowly decline during the 2.3 seconds after extinguishing the light.

Elucidation of the Mechanism Responsible for OEEC

In Figures 17A and 17B, the magnitude of the peaks at $m/z = 108$ are nearly identical. This observation is convincing evidence that the Q monomer cannot itself be responsible for OEEC. In the previous two experiments, the peak at $m/z = 216$ corresponds to Q_2^- , the negative ion of a dimer of Q. The formation of Q_2^- in the presence of UV radiation is thought to be responsible for the OEEC response observed in the PDM-ECD. Although the peak at $m/z = 216$ is large in Figure 17B, it only represents slightly more than a twofold increase in ion signal relative to the response without light ($RE \approx 2$). A value of $RE \approx 7$ was determined for Q by the PDM-ECD. The difference between the RE values from the two instruments is not unexpected and is attributed to two factors. First, the geometry of the APIMS ion source is such that a significant portion of the rear ionization volume is not accessible by the light. Second, the nature of the signal

detection methods for the two instruments are quite different. The PDM-ECD measures a decrease in electron current at a positively charged pin located within the source, while the APIMS measures an increase in ion current at a secondary electron multiplier (channeltron) located outside of the ion source.

Q_2^- could be produced in the ion source by several different processes. Following normal EC, a quinone anion could associate with a neutral quinone molecule to form the cluster anion, $Q^-(Q)$. However, if this species were formed readily in the ion source, it should be present both with and without irradiation. Because the peak at $m/z = 216$ is only visible during irradiation, formation of $Q^-(Q)$ is not indicated.

It was discussed previously that the process responsible for OEEC involves electronic excitation of the neutral quinone molecules. Excimer formation is one process that relies on neutral photoexcitation to form a dimer. It is conceivable that a gas-phase triplet excimer, Q^*Q , could be produced from two molecules of Q in the presence of UV light. (If an excimer form of Q were formed, it would probably be from ${}^3Q^*$ rather than ${}^1Q^*$, because intersystem crossing to produce ${}^3Q^*$ is thought to proceed with unit efficiency (69), and ${}^3Q^*$ has a fairly long lifetime of 28.4 μs (65).) In order to detect the

excimer in the PDM-ECD or APIMS, the lifetime of Q^*Q against deactivation must be longer than its lifetime against EC. The minimum lifetime against EC for a compound in the PDM-ECD can be estimated from the inverse of the pseudo-first-order rate constant for EC, $k_{ec}[e^-]$. The largest values for k_{ec} are about $5 \times 10^{-7} \text{ cm}^3 \text{ molec}^{-1} \text{ sec}^{-1}$ (22), and the concentration of electrons within the ion source is about $10^8 \text{ e}^- \text{ cm}^{-3}$. This leads to a minimum lifetime against EC of 20 ms. Data from Hunter and Stock (70) show that gas-phase triplet-state benzene has a lifetime of 590 μs , while the lifetime of the gas-phase triplet excimer of benzene is less than 0.1 μs . If the behavior of Q is even remotely similar to that of benzene, the lifetime of the triplet state excimer would be too short against deactivation to undergo EC.

Another process involving neutral photoexcitation that could result in a dimer is photoaddition. Both the necessary minimum lifetime against EC of 20 ms, and the slow decline of the peak at $m/z = 216$ in Figure 19B-E suggests that the EC-active species is a stable molecular dimer of Q, Q_2 . The photochemical process thought to be responsible for the production of Q_2^- is shown as Reactions



24a-c. This process involves absorption of a photon by Q to form the excited neutral, Q^* . The dimer is then formed by Reaction 24b, a photocycloaddition between Q^* and a neutral molecule of Q in the ground state. Finally, the stable molecular dimer captures an electron by the resonance EC mechanism, Reaction 24c.

The proposed explanation for the OEEC response observed for Q is that the EC rate constant for Q_2 is several orders of magnitude greater than that for Q. An important fact that was previously mentioned with regard to formation of Q^- from Q is the large negative entropy associated with the process due to the large geometry difference between the anion and the neutral. If the Franck-Condon factors for production of Q_2^- from Q_2 are more favorable than they are for the monomer, the EC rate constant might be significantly higher for Q_2 than for Q. Along with this fact, the presence of the two additional electron-withdrawing oxygens in the dimer may result in a higher electron affinity (55) in the dimer than in the monomer. It is believed that OEEC by MQ, DMQ and TMQ is also due to the formation of dimers by mechanisms analogous to Reactions 24a-c. It is also thought that MQ_2 , DMQ_2 and TMQ_2 have significantly higher electron capture rate constants than the monomers.

It is important to determine whether the above mechanism is kinetically feasible. Using collision theory of bimolecular reactions in the gas phase, it is possible to estimate an upper limit for the rate constant, k_{Q^*Q} , in Reaction 24b. Assuming unit collision efficiency, a rate constant of $\approx 2 \times 10^{-10} \text{ cm}^3 \text{ molec}^{-1} \text{ sec}^{-1}$ is calculated for k_{Q^*Q} from equation 25 (35), where the collision cross

$$k_{Q^*Q} = \sigma \left(\frac{8kT}{\pi\mu} \right)^{\frac{1}{2}} N_A \quad (25)$$

section, σ , is given by $\pi(2R_Q)^2$ and N_A is Avogadro's number. From k_{Q^*Q} and the estimated concentration of Q within the ion source, the lifetime of Q^* against dimerization can be calculated and compared to the known lifetime of Q^* against relaxation. In the APIMS experiments, the concentration of Q within the source at the peak maximum is estimated to be $4 \times 10^{15} \text{ molec cm}^{-3}$ (the estimated concentration of Q was calculated according to the method discussed in Experimental). This leads to a value of $\approx 1 \times 10^{-6} \text{ sec}$ for the lifetime of Q^* against dimerization. The lifetime of Q^* against relaxation is $3 \times 10^{-5} \text{ sec}$ (65). Because the lifetime of Q^* against dimerization is estimated to be shorter than that for relaxation, the mechanism proposed above is thought to be kinetically feasible.

The above mechanism helps to explain several previous observations made with the PDM-ECD and the APIMS. In Figure 10, the RE values were seen to increase steadily with increasing concentration of Q. Christophorou and coworkers made a similar observation in an electron swarm experiment (71). They observed optically enhanced electron attachment to thiophenol following laser irradiation and noticed that this enhancement increased with increasing thiophenol concentration. They attributed their observations to the formation of diphenyl disulfide, PhSSPh, from two thiophenoxy radicals, and subsequent electron attachment to form PhSSPh⁻. (The thiophenoxy radicals were formed as a result of the laser pulse by photofragmentation of the thiophenol molecules.) Reactions 24b and 24c are similar to the mechanism proposed by Christophorou in that they require two quinone molecules to produce Q₂, which is responsible for OEEC. The appearance of the single ion chromatograms in Figure 18 is due to the same concentration dependence. The signal for m/z = 216 does not begin to rise until the concentration of Q in the ion source is sufficiently high, and at this point, it increases rapidly. When the Q concentration begins to slowly drop, the signal due to Q₂⁻ decreases quickly.

In Figure 19, it was previously noted that the peak at $m/z = 216$ slowly declined after extinguishing the light. Ventilation of Q_2 from the ion source is thought to be responsible for this observation. In a comparable experiment, Christophorou (71) noticed that the enhanced electron attachment decreased as the time delay between the laser pulse and the arrival of the electron swarm increased. This was attributed to diffusion of PhSSPh out of the interaction region, a process analogous to ventilation from the APIMS ion source.

In Figure 15, the peak at 240 nm in the OEEC spectrum of Q was previously observed to be an order of magnitude larger than the corresponding peaks for the methylated quinones. A combination of several different factors could explain this observation. The EC rate constants for the quinone monomers were reported by Mock and Grimsrud (19) and are shown in Table 2. Also shown is the largest rel σ_{OEEC} measured by the PDM-ECD for each quinone.

The difference in rel σ_{OEEC} between Q and its methylated derivatives is thought to be primarily caused by their different EC rate coefficients. From Table 2, the EC rate coefficient for Q is seen to be more than an order of magnitude smaller than the coefficients for MQ, DMQ and TMQ.

Table 2.

EC Rate Coefficients for the Quinone Molecules

	Q	MQ	DMQ	TMQ
k_{ec} , ^a $\text{cm}^3 \text{s}^{-1}$	1.5×10^{-14}	3.5×10^{-13}	8×10^{-13}	3.5×10^{-12}
rel σ_{OEEC} ^b	7.8	0.58	0.19	0.42

^a EC rate coefficients of ground state quinones at 180°C from reference 19.

^b Relative optically enhanced electron capture cross section taken from results shown in Figure 15.

If the EC rate coefficients for the quinone dimers are all of similar magnitude, Q should exhibit the largest OEEC response of the quinones because it has the smallest EC rate coefficient of the quinone monomers. Another factor may also influence the magnitudes of the OEEC responses for the quinones. It is conceivable that MQ₂, DMQ₂ and TMQ₂ are not formed as easily as Q₂ due to steric effects during the interaction of the methylated quinone monomers to form the dimers. A difficulty in producing the methylated dimers could result in the large response for Q observed in Figure 15.

Possible Structures of the Dimers. Several researchers have synthesized dimers of Q (72, 73) and DMQ (74) by liquid phase photolysis or by irradiation in the solid state. Two similar structures for Q₂ have been

reported. Structure I in Figure 20, the cage dimer, is formed by successive 2+2 additions across the olefinic linkages and contains two cyclobutane rings (72). Structure II, the trans open dimer, contains only one cyclobutane ring (73). Although the cis dimer has not previously been reported, it is shown as structure III. DMQ₂ has been synthesized and has been shown to have the spiro-oxetan form of structure IV (74). The spiro-oxetan is formed by the addition of the carbonyl group of one molecule to the olefinic linkage of the other.

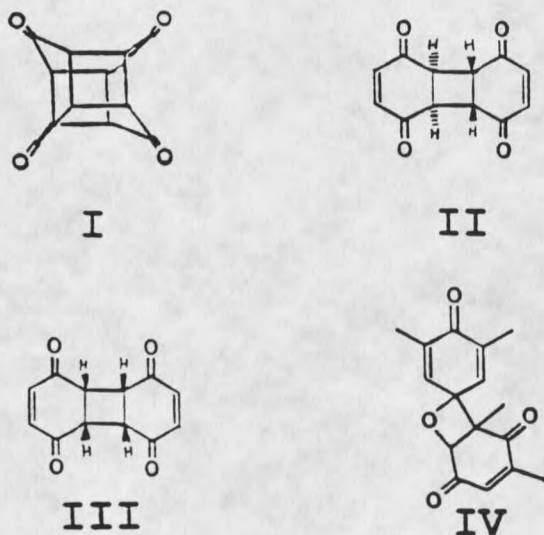


Figure 20. Possible structures of the dimers of Q and DMQ. Structures I (72), II (73) and IV (74) have been reported in the literature.

PDM-ECD Study of Iodide-WaterClustering Equilibria

In the Introduction, the use of PD for a wide range of thermochemical measurements was discussed. Although PD has been used to probe the properties of simple atomic and molecular anions, the technique has been used sparingly to obtain thermochemical information about ion clustering reactions. The analytical applications of negative ion clustering in the PDM-ECD were recently investigated (32, 33), and the results suggested that the instrument would be useful for more fundamental studies.

In Theory, it was shown that at atmospheric pressure, ion-molecule reactions readily attain a state of chemical equilibrium within the ionization volume of the PDM-ECD. For an ion clustering reaction, if the concentrations of the reactants and products within the ionization volume can be experimentally measured, information about the established equilibrium can be determined.

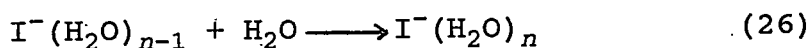
This section describes the utility of the PDM-ECD for the study of iodide-water clustering equilibria. The presence of water and the effects of different temperatures on the response of the PDM-ECD to I^- will be shown and discussed. The PD spectra of I^- under dry and wet conditions will also be shown and discussed.

Response of PDM-ECD to Iodide

With Water Present

In the initial phase of these studies, it was necessary to understand how the presence of water affected the response of the PDM-ECD to iodide. Figure 21 shows two sets of chromatograms of CH_3I recorded with 380 nm light from the Xe lamp and an ECD temperature of 130°C . Light at this wavelength is expected to cause PD from I^- (75). In both cases, the top chromatogram provides the EC response, $\delta I_{L/C}$, while the bottom chromatogram provides the PD-modulated response, δI_M . The only difference in experimental conditions is that the chromatograms on the right were obtained simultaneously with very dry carrier and buffer gases, while those on the left were obtained with 3.9 torr water present in the detector gas.

It is apparent from Figure 21 that the magnitude of the δI_M response with water present is somewhat diminished with respect to the dry system. The same effect was observed by Arbon and Grimsrud (32) in a similar instrument but which lacked a monochromator. This effect was thought to be due to the iodide-water clustering equilibrium shown in Reaction 26. The equilibrium



clustering reactions of the halides with water have been studied extensively by Magnera et al. (76) and Hiraoka et

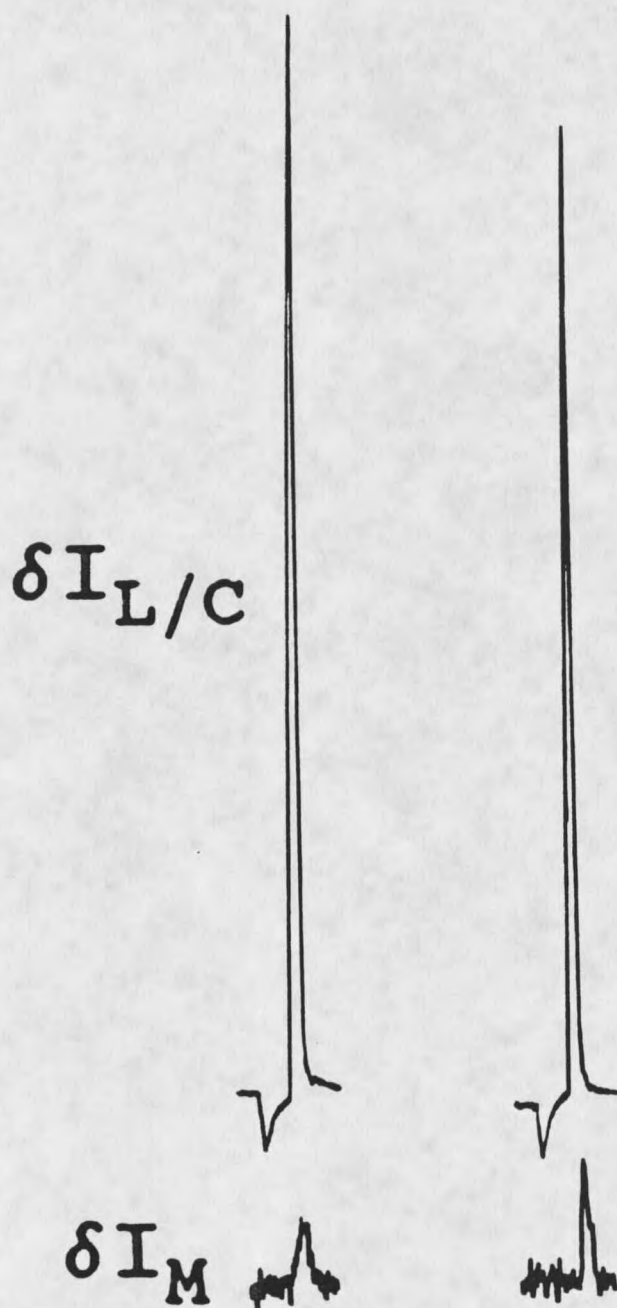


Figure 21.

PDM-ECD chromatograms of CH_3I at 130°C and with the monochromator set at 380 nm. δI_M is the PD-modulated response, while $\delta I_{L/C}$ is the EC response. The chromatogram on the left was obtained with 3.9 torr of H_2O in the detector gas, while the chromatogram on the right was recorded under dry conditions.

et al. (77). The more recent report of Hiraoka et al. included thermochemical and equilibria data for Reaction 26 with $n = 1-5$. All of the predicted values that are used to make comparisons with PDM-ECD data are calculated from this report. These thermochemical data include enthalpies and entropies of solvation for each successive clustering reaction. From these values, it is possible to calculate relative abundances of the clustered iodide ions at equilibrium. With no water present, all of the iodide produced by EC is expected to exist as I^- . However, at a temperature of 130°C and with 3.9 torr water present, equilibrium calculations (77) predict that approximately 50% of the iodide will exist as I^- , 45% as $I^-(\text{H}_2\text{O})$ and 5% as $I^-(\text{H}_2\text{O})_2$.

It has recently been shown (28-31) that the PD threshold of a clustered anion is shifted to shorter wavelengths relative to that for the unclustered anion. The magnitude of the shift is approximately equal to the solvation energy of the cluster. This topic will be discussed in more detail in a later section. The enthalpy of solvation for Reaction 26 where $n=1$ is -10.3 kcal (77). Because the $I^-(\text{H}_2\text{O})$ is stabilized by 10.3 kcal relative to I^- , the onset for PD is expected to be blue-shifted by approximately this amount of energy. This corresponds to a PD onset for $I^-(\text{H}_2\text{O})$ of 353 nm (PD onset for I^- is 405

nm (75)). Therefore, with the monochromator set at 380 nm, the only iodide-containing species present in the ionization volume that will undergo PD is the free, unclustered form. With water present, the concentration of I^- is diminished by participation in Reaction 26, and therefore, the δI_M response in Figure 21 is smaller when water is present than it is in a dry system.

Relative Abundances of Iodide-Water Clusters

From PDM-ECD Measurements

Mock et al. showed that the magnitude of the $\delta I_{L/C}$ response is proportional to the amount of I^- produced by EC (9, 18). The magnitudes of the δI_M responses in Figure 21 are thought to be proportional to the amount of unclustered I^- present in the ionization volume after Reaction 26 has reached equilibrium. By normalizing the PD-modulated response according to Equation 27, different

$$\delta I_M / \delta I_{L/C}, \quad (27)$$

chromatograms can be compared quantitatively and the responses of the PDM-ECD can be used to calculate experimental relative abundances for I^- and $I^-(H_2O)_n$. Using Equation 27, the chromatograms in Figure 21 give normalized responses for dry and wet conditions of 0.011 and 0.0064 respectively. The first value is thought to be proportional to the total concentration of all iodide-containing species, while the second value corresponds to

the concentration of unclustered I^- only. With this treatment of the data, the equilibrium concentration of I^- in the ionization volume of the PDM-ECD at 130°C and with 3.9 torr water is calculated from Figure 21 to be 58%. This is in good agreement with the above predicted value of 50%. The total concentration of all clustered forms of iodide, $I^-(\text{H}_2\text{O})_n$, is calculated from Figure 21 to be 42%.

Mock and Grimsrud (11) have shown that the PD cross section for I^- is independent of temperature from 100°C to 190°C . Therefore, valid comparisons at temperatures in this range can be made with the chromatogram taken under dry conditions at 130°C in Figure 21. Additional PDM-ECD measurements were made at temperatures from 130°C to 190°C under conditions identical to those in Figure 21. From these data, the relative abundances of I^- and $I^-(\text{H}_2\text{O})_n$ are plotted as a function of temperature in Figure 22. For comparison, the smooth curves are the predicted abundances of the cluster ions which were calculated from the thermodynamic parameters of Hiraoka et al. (77). Throughout the temperature range of the study, it can be seen that the I^- abundances calculated from the PDM-ECD measurements are somewhat greater than the predicted values, while the abundances of $I^-(\text{H}_2\text{O})_n$ are slightly less than the predicted values for $I^-(\text{H}_2\text{O})$. However, the

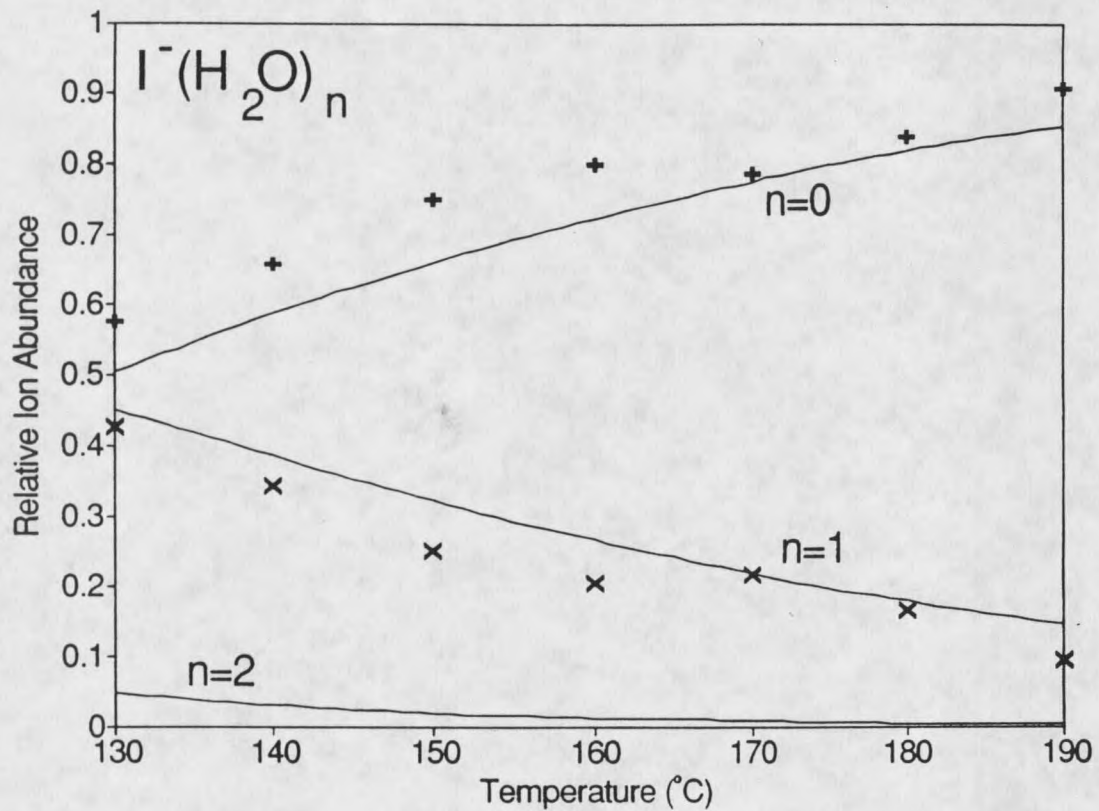


Figure 22. Relative abundances of I^- and $I^-(H_2O)_n$ from 130-190°C with 3.9 torr H_2O present in the detector gas. The smooth curves are the predicted abundances of $(H_2O)_n$ from Hiraoka (77). The PDM-ECD data is represented by (+) $n=0$ and (x) $n=1$.

overall appearances of the two sets of data are very similar.

Determination of Equilibrium Constants and Thermochemical Data for the Iodide-Water Clustering Reaction

The predicted cluster distributions at equilibrium from Figure 22 show that at temperatures of 130°C and above and with 3.9 torr water, very little iodide should exist in the form, $I^-(H_2O)_2$. With the approximation that all iodide is either unclustered or is present as $I^-(H_2O)$, it is possible at 130°C to estimate the equilibrium constant, $K_{0,1}$, for Reaction 26, where $n=1$. Using the previously calculated value of 58% I^- and assuming 42% $I^-(H_2O)$, $K_{0,1}$ at 130°C and with 3.9 torr water is found to be 141 atm^{-1} . The main source of uncertainty in the calculation of $K_{0,1}$ is in the noise associated with δI_M from pen 2. In Figure 21, noise comprises approximately 30% of the δI_M response for the wet system and 17% for the dry system. Calculating the propagation of error for the determination of $K_{0,1}$ results in a potential error of 60%. It is therefore encouraging that the reported result for $K_{0,1}$, $141 \pm 84 \text{ atm}^{-1}$, compares fairly well with 174 atm^{-1} which is the predicted value for $K_{0,1}$ at 130°C (77). The propagation of error discussed above is dramatically worse for the measurements at higher temperatures. Therefore,

it is not possible to calculate $K_{0,1}$ for these measurements.

Comparison of the PD Spectra of I^- Under
Dry and Wet Conditions

The results of the previous sections depend to a great extent on the premise that the PD threshold for $I^-(H_2O)$ is significantly blue-shifted with respect to that for I^- . It should be possible to determine whether this assumption is valid by measuring the wavelength dependence of the PD cross section for the iodide-water system. Mock and Grimsrud (10-12, 18) showed that the PDM-ECD functions well for determination of PD spectra of both atomic and molecular negative ions. If the PD cross section of $I^-(H_2O)$ is of sufficient magnitude and is distinct from that of I^- , it should be possible to obtain qualitative information about the PD spectrum of $I^-(H_2O)$.

In Figure 23, the PDM-ECD was used to obtain the PD spectra of I^- under dry and wet conditions. Curve A shows the PD spectrum of I^- at 100°C with very dry carrier and buffer gases. This spectrum consists of a sharp onset starting at about 410 nm, and relatively constant cross sections between 385 and 310 nm. As shown by curve B, significant changes in the PD spectrum are caused by the presence of 1.9 torr water in the ionization volume. Like curve A, curve B shows an onset for PD at about 410 nm,

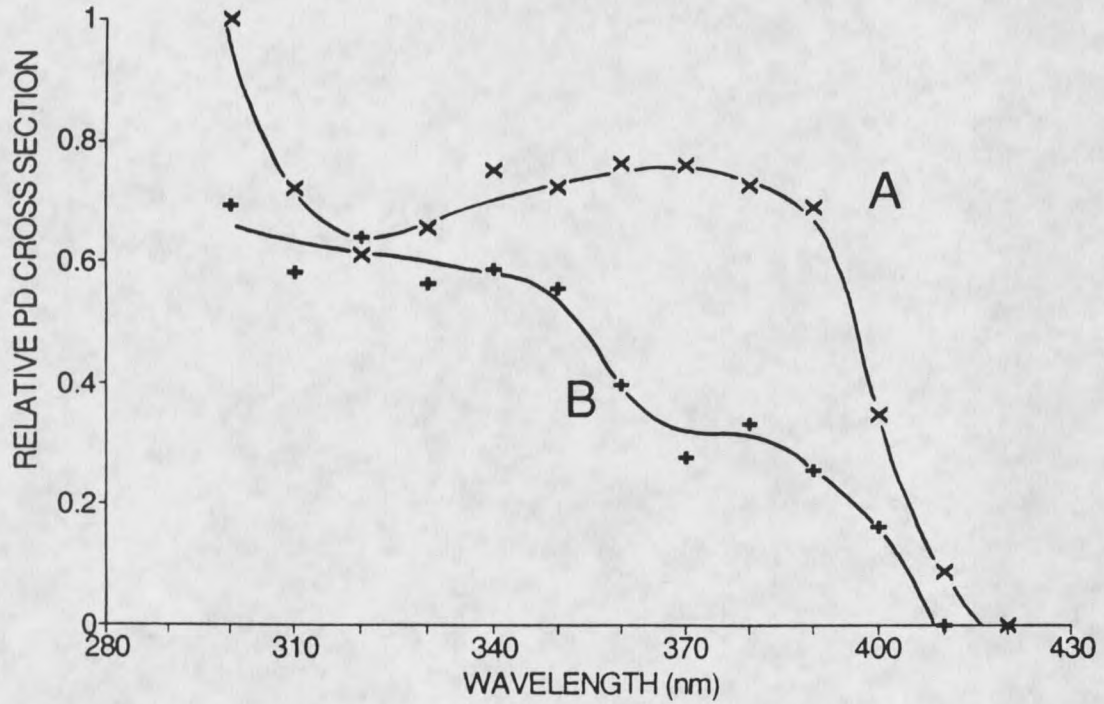


Figure 23. PD spectra of I^- at 100°C (A) with dry carrier and buffer gas and (B) with 1.9 torr H_2O present in the detector gas.

due to the presence of I^- . However, the PDM-ECD response at 380 nm is roughly half as large as in curve A. This implies that only about half of the total iodide exists as I^- after Reaction 26 has reached equilibrium. For comparison, equilibrium calculations predict that 55% of the total iodide should exist as I^- under these conditions (77). An increase in the PD cross section is observed at about 360 nm in curve B, and this is thought to be due to the onset of PD for $I^-(H_2O)$.

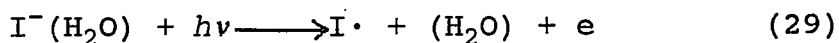
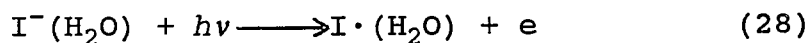
There is only one previous PD study of a hydrated anion with which to compare these spectra. Golub and Steiner (78) recorded the first PD spectrum of a clustered anion when they studied $OH^-(H_2O)$ in a crossed beam apparatus. The mass-selected cluster ion was irradiated by light of 20 nm bandwidth. They observed a PD onset at 2.95 eV (420 nm) and a slowly rising cross section over 1 eV. The slow rise was attributed to dissociative PD in which $\cdot OH$ and H_2O were produced as separate neutrals. Branscomb (79) recorded the PD spectrum of OH^- in a crossed beam apparatus with light of 5 nm bandwidth. The PD onset was observed at 1.83 eV (677 nm) and the cross section was seen to rise sharply in this region.

Although the PD spectrum in curve B of Figure 23 is due to both I^- and $I^-(H_2O)$, an important similarity exists between it and the PD spectra of OH^- and $OH^-(H_2O)$. In

both the PDM-ECD and the crossed-beam studies, the PD onset for the clustered species was blue-shifted by an energy approximately equal to the enthalpy of solvation. For OH^- and $\text{OH}^-(\text{H}_2\text{O})$, the shift of $25.8 \text{ kcal mol}^{-1}$ (1.12 eV) is consistent with ΔH of 25 kcal mol^{-1} (80). For I^- and $\text{I}^-(\text{H}_2\text{O})$, the shift from 410 nm to 360 nm corresponds to 10 kcal mol^{-1} , which agrees well with the value of $10.3 \text{ kcal mol}^{-1}$ obtained from ion cluster equilibrium studies (77). The calculation of ΔH and the significance of the PD products for $\text{I}^-(\text{H}_2\text{O})$ will be discussed in the next section.

Determination of ΔH From PD Spectra

From PD data analogous to those in Figure 23, Coe et al. (28-30) and Moylan et al. (31) have computed ΔH values for ion-molecule clustering reactions similar to the iodide-water system. To properly calculate ΔH from these data, it is necessary to know what species might be produced by PD of the clustered ion and whether the possible products differ significantly in energy. For the iodide-water system, two schemes are possible. In Reaction 28, PD is envisioned to produce a free electron



plus the neutral cluster, $\text{I}\cdot(\text{H}_2\text{O})$. In Reaction 29, the generation of dissociated $\text{I}\cdot$ and H_2O is shown. The

difference in energy between the neutral cluster and the dissociated neutrals is the neutral binding energy (NBE). For $I\cdot$ and H_2O , a NBE value of $0.45 \text{ kcal mol}^{-1}$ was calculated using MOPAC 6.00 with AM1. Because the NBE value is so small, the energy difference between the possible products of Reactions 28 and 29 is also small. Therefore, a good approximation of ΔH can be made without regard to the PD products simply by measuring the difference in energy between the PD onsets for I^- and $I^-(H_2O)$. The ΔH value of about $-10 \text{ kcal mol}^{-1}$, which was previously determined from Figure 23, is therefore a valid approximation.

Kinetics of Gas-Phase S_N2 Reactions of Alkyl Bromides With Chloride

Bimolecular nucleophilic displacement (S_N2) reactions have been studied extensively in solution and are among the most powerful and widely used synthetic reactions in organic chemistry (81, 82). The study of S_N2 reactions has revealed important information about a variety of organic reaction phenomena, including steric and polar effects, correlations between structure and reactivity, thermodynamics, and kinetics (83, 84).

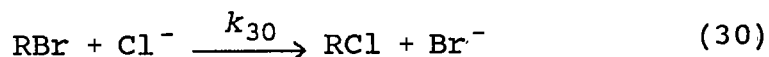
Kinetic investigations have been central to an understanding of nucleophilic displacement reactions, ever

since the early work by Ingold *et al.* on S_N2 reaction mechanisms in solution (85-87). Kinetic studies in the gas phase during the last 20 years have revealed a wealth of information about basic reactivity in S_N2 displacement without the presence of solvent. Researchers have studied intrinsic nucleophilicity (83), competition between E2 and S_N2 reactions (16), temperature dependence of S_N2 rate constants (14), and agreement between experiments and theoretical predictions (88). However, almost all of these investigations have been performed at relatively low total pressures. As it was illustrated in the Introduction by the reaction of Cl^- with CH_3Br , measurements over a wide pressure range are important to a more complete understanding of GPIC.

This section describes a kinetic study of S_N2 displacement at atmospheric pressure. The PDM-ECD will be used to study the reactions between chloride and 20 alkyl bromides. The response of the instrument will be characterized and the methods for measurement of the S_N2 rate constants will be explained. The rate constants for the reactions at 125° will be listed, intercompared, and compared with previous results. Finally, the temperature dependence of the S_N2 rate constants for the reactions of bromomethane and 2-bromopropane with chloride will be listed and compared with previous results.

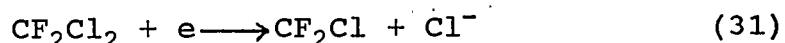
Introduction of Reactants and Monitoring
of S_N2 Displacement

S_N2 displacement of an alkyl bromide (RBr) with chloride is shown in Reaction 30. In order to induce



this reaction in the PDM-ECD, the nucleophile, Cl⁻, must be generated and the alkyl bromide substrate must be introduced. In addition, it must be established that the reaction can be monitored within the PDM-ECD.

Cl⁻ was produced from CF₂Cl₂ by dissociative electron capture, Reaction 31. As described in Experimental, a



small concentration of CF₂Cl₂ was permanently present in the make-up gas of the PDM-ECD. The introduction of CF₂Cl₂ was carefully controlled to provide a stable population of electrons and Cl⁻ ions in the cell.

The alkyl bromides were introduced to the PDM-ECD by a gas chromatograph, and were thereby separated from potential impurities. The retention times of most of the compounds were determined by parallel chromatographic studies with flame ionization detection (FID). However, a few of the alkyl bromides required additional identification procedures. The FID chromatograms of 1-bromo-2-methylpropane (1B2MPR), 2-bromobutane (2BB), and

bromocyclopropane (BCPR) were observed to contain several significant peaks. For these compounds, the chromatographic peak corresponding to the alkyl bromide of interest was determined by GC-MS.

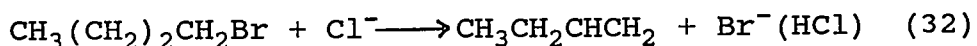
The case of (bromomethyl)cyclopropane (BMCPR) nicely demonstrates the advantage of chromatographic introduction in the study of GPIC. The FID chromatogram showed two small impurity peaks and one large peak due to BMCPR. Analysis by GC-MS, followed by a mass spectral library search revealed that the two impurities were monobromobutenes with the same mass as BMCPR. Serious errors would be expected if this compound were introduced without chromatographic separation and its reactions studied by traditional mass spectrometric GPIC techniques.

S_N2 displacement was monitored by the photodetachment response of the PDM-ECD. The threshold for PD from Br^- is 375 nm, while the PD threshold for Cl^- is 345 nm (89). In order to provide a selective response to Br^- without interference from Cl^- , the intense emission at 365 nm of the Hg-Xe lamp was selected by the monochromator. All of the alkyl bromides that were studied show no measurable electron capture response at the concentrations that were used. Therefore, only Br^- produced by Reaction 30 underwent PD at 365 nm.

Experimental Measurement of S_N2 Displacement

Figure 24 shows the PDM-ECD response to 13 ppm of 1-bromobutane (1BB) at 125°C with Cl⁻ present in the ECD according to the conditions described above. The PD and EC chromatograms were obtained simultaneously as described in Experimental. In concert with the above observation that the alkyl bromides do not appreciably capture electrons, no EC response for 1BB is seen in Figure 24. Therefore the amount of Br⁻ produced by electron attachment to 1BB is exceedingly small. A PD response is observed, however, and this is thought to be due to the conversion of Cl⁻ to Br⁻ by Reaction 30 (where RBr = 1BB).

It is not by any means certain that the reaction measured in Figure 24 is S_N2 displacement. Kebarle *et al.* (14, 90) have pointed out that the same reactants could produce Br⁻ in the gas phase by the bimolecular elimination mechanism (E2). The simple concerted E2 reaction in which an olefin, and separated HCl and Br⁻ are produced is endothermic by 5-10 kcal mol⁻¹ in the gas phase (14). However, the E2 process could be envisioned to occur by Reaction 32, with subsequent dissociation of



the clustered intermediate, Br⁻(HCl), to Br⁻ and HCl. Reaction 32 is thought to be exothermic by a few kcal mol⁻¹ (90). In a number of studies involving E2 and S_N2

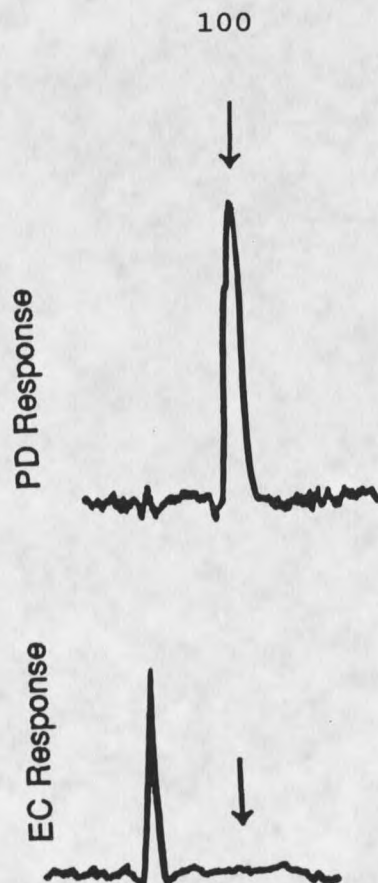


Figure 24.

Response of the PDM-ECD to 1-bromobutane (1BB) chromatographically introduced to the detector at the time indicated by the two arrows. The detector gas contains a stable concentration of Cl^- . No significant EC response to 1BB is observed. 365 nm light was used to obtain the PD response. The PD response is due to Br^- produced by an $\text{S}_{\text{N}}2$ reaction between Cl^- and 1BB. The large peak in the EC response is due to small amounts of oxygen introduced with the sample. Temperature is 125°C .

reactions, clustered intermediates were only seen when strong nucleophiles were used; $\text{Br}^-(\text{HCl})$ has not been observed (14, 16).

In another experiment with bromoethane (BE) instead of 1BB, the PD responses due to Br^- produced by Reaction 30 are plotted against the concentration of BE in the ECD (the ECD concentration of BE was calculated according to the method discussed in Experimental). The resulting graph is shown in Figure 25. As the concentration of BE is varied from zero to the highest values indicated, the fraction of Cl^- that is converted to Br^- increases continuously. At relatively high concentrations of BE, a saturation level is approached in which the conversion of Cl^- to Br^- is almost complete in the steady state. The saturation level in Figure 25 was determined experimentally to be 9.6 pA and corresponds directly to $[\text{Cl}^-]_0$, the relative amount of Cl^- that is continuously maintained in the cell without BE present. The uncertainty in $[\text{Cl}^-]_0$ is estimated to be about 7% and is due to baseline noise in the PD chromatogram.

At a given concentration of BE, the relative concentrations of Br^- and Cl^- in the ECD can be easily deduced from $[\text{Cl}^-]_0$ and the PD response. Mock and Grimsrud showed that the magnitude of the PD response is proportional to the amount of negative ions produced

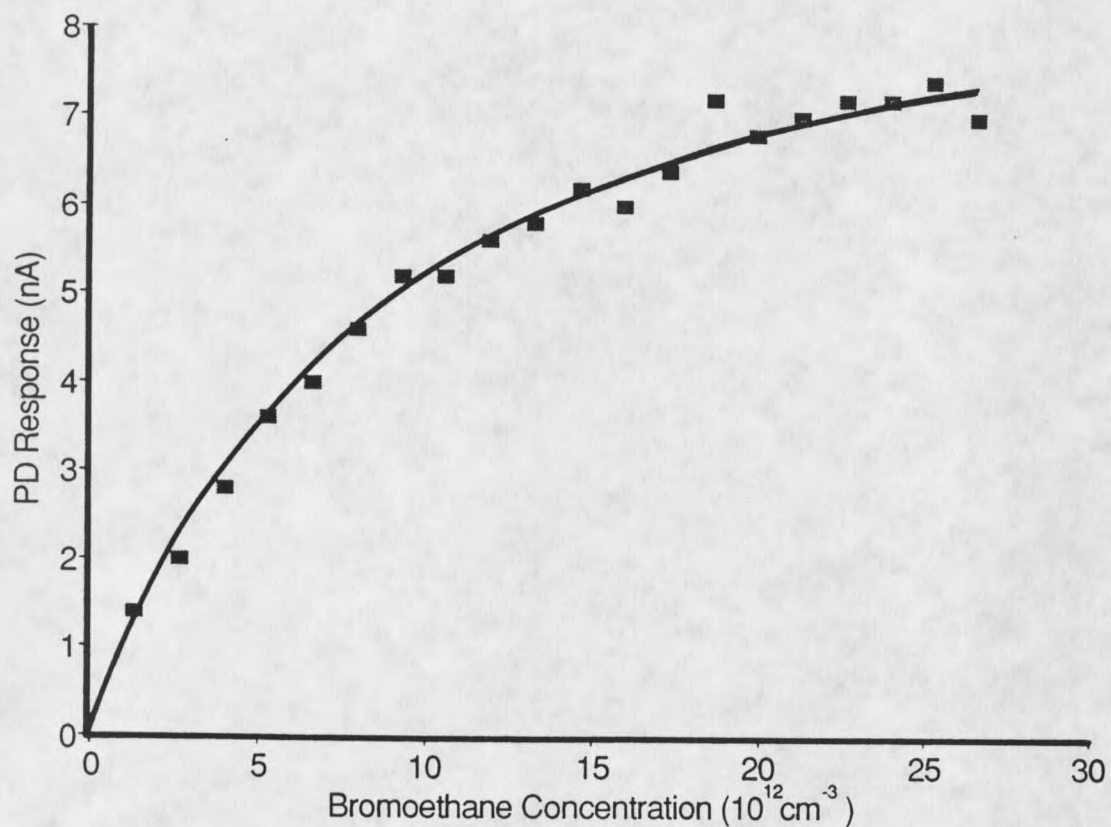


Figure 25.

A plot of the magnitudes of the PD responses as a function of the concentration of bromoethane in the detector at the peak maxima. The PD measurements were recorded in experiments of the type shown in Figure 24.

in the cell (18). The relative amount of Br^- produced from BE by Reaction 30 is therefore proportional to the PD response in Figure 25. Cl^- is removed from the cell by reaction 30 as Br^- is produced. It follows that the relative amount of Cl^- present in the cell at a given concentration of BE is proportional to the difference between $[\text{Cl}^-]_0$ and the PD response. The above relationships are summarized in Equations 33a and 33b.

$$[\text{Br}^-] \propto \text{PD response} \quad (33a)$$

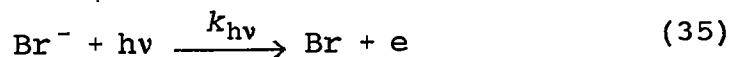
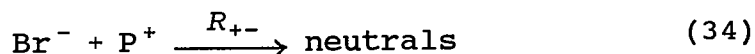
$$[\text{Cl}^-] \propto [\text{Cl}^-]_0 - \text{PD response} \quad (33b)$$

As the PD response approaches the saturation level, the uncertainty in $[\text{Cl}^-]$ calculated from Equation 33b increases dramatically because of the uncertainty in $[\text{Cl}^-]_0$ described above.

Derivation of $\text{S}_{\text{N}}2$ Rate Law

From concentration measurements like the ones shown in Figure 25, and from a simple model of all of the reactions thought to be occurring in the cell, the rate constant for Reaction 30, k_{30} , can be calculated. Under the conditions described above, the reactions responsible for the production and loss of Br^- are $\text{S}_{\text{N}}2$ displacement, Reaction 30, ion-ion recombination, Reaction 34, and

photodetachment, Reaction 35. With identical optical



conditions, Mock and Grimsrud reasoned that negative ion destruction due to photodetachment would be negligible in comparison with ion-ion recombination (11). From Reactions 30 and 34, the rate expression shown in Equation 36 can be derived. It is reasonable to assume the steady

$$\frac{d[\text{Br}^-]}{dt} = k_{30}[\text{Cl}^-][\text{RBr}] - R_{+-}[\text{P}^+][\text{Br}^-] = 0 \quad (36)$$

state approximation with regards to Br^- because the production and loss mechanisms are very fast on the time scale of the experimental measurement (91). The above rate expression can be simplified to the rate law shown in Equation 37. The collective term $R_{+-}[\text{P}^+]$, the pseudo-

$$\frac{[\text{Br}^-]}{[\text{Cl}^-]} = \frac{k_{30}[\text{RBr}]}{R_{+-}[\text{P}^+]} \quad (37)$$

first-order rate constant for ion-ion recombination, was discussed in Theory and has been determined to be equal to $100 \pm 50 \text{ s}^{-1}$ under these conditions (18). Equation 37 therefore provides a straightforward method for calculation of k_{30} from experimental data of the type shown in Figure 25.

Procedure for Measurement of S_N2 Rate Constants

In order to use Equation 37 to determine k_{30} , the following experiments must be performed: the PD saturation level must be established, a usable range of RBr concentrations must be determined, and the PD responses at these concentrations must be measured.

First, for every set of concentration vs. PD measurements, the saturation level, $[Cl^-]_0$, must be determined. Figure 26 shows injections of four different concentrations of 1-bromobutane (1BB). The first chromatogram shows a response below the saturation level due to an injection of 6 ppm 1BB. The PD responses to 20, 30, and 40 ppm injections of 1BB are nearly identical, and correspond to the saturation level. Interestingly, the EC response for the 40 ppm injection shows a small peak above the noise due to formation of Br^- by dissociative electron capture. However, this additional production of a small amount of Br^- by EC does not appear to affect the magnitude of the PD response.

Injections of 30 ppm of 1BB or 40 ng of 1-bromopentane were used to determine the saturation level. Measurements of the saturation level were repeated for each set of experimental data in order to account for small variations in light intensity, gas flow through the cell, and CF_2Cl_2 concentration in the make-up gas.

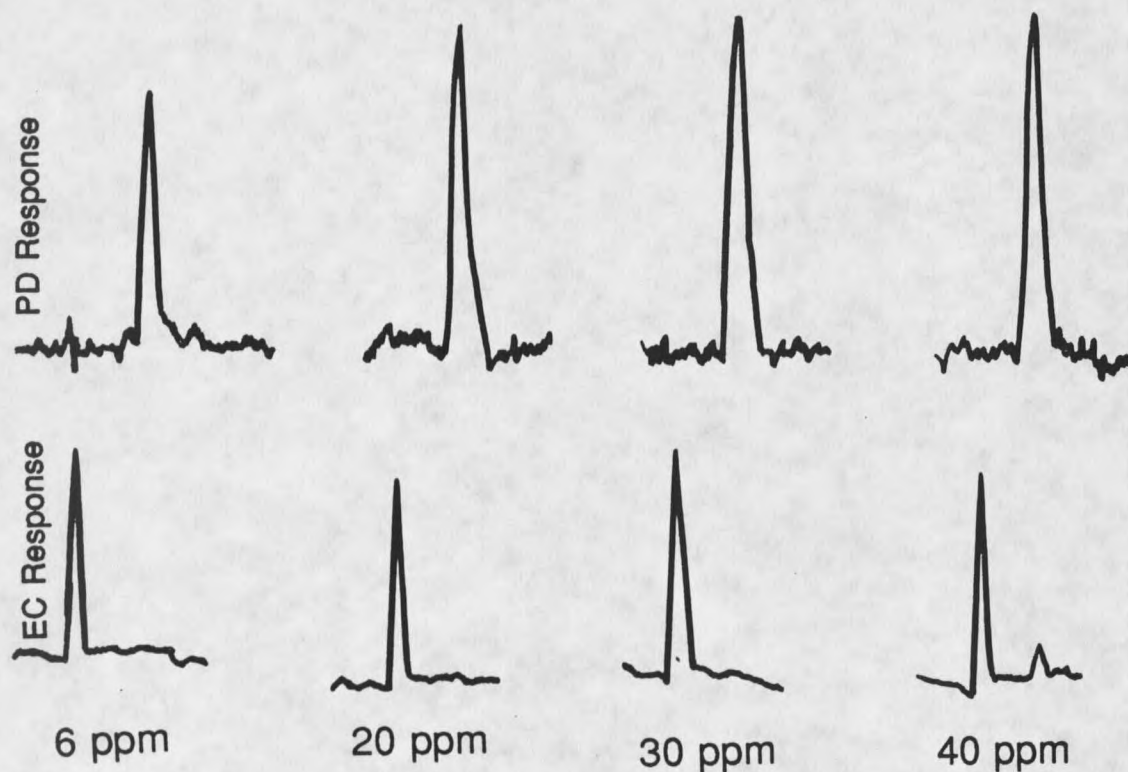


Figure 26.

Response of the PDM-ECD to different concentrations of 1-bromobutane (1BB). The injection of 6 ppm of 1BB elicits a PD response below the saturation level, which is indicated by injections of 20, 30, and 40 ppm of 1BB. The small EC response observed after the injection of 40 ppm is due to the production of Br^- by dissociative electron capture.

After the saturation level is determined, a usable concentration range for the alkyl bromide of interest must be established. As it was explained previously, the uncertainty in $[Cl^-]$ determined from Equation 33b increases dramatically as the saturation level is approached. For this reason, the alkyl bromide concentrations that are used to plot Equation 37 are always below 75% of saturation. After this upper concentration limit is found, the lowest concentration of RBr that gives a measurable PD response is determined.

Experimental data of PD response vs. $[RBr]$ are gathered between the two concentration limits and graphed as shown in Figure 25. From the PD responses, $[Br^-]$ and $[Cl^-]$ are calculated from Equations 33a and 33b and plotted vs. $[RBr]$. Using $[Br^-]/[Cl^-]$ as the dependent variable, and $[RBr]$ as the independent variable, a least-squares fit of the data gives a line of slope = $k_{30}/R_{+-}[P^+]$, according to Equation 37.

Results of Rate Constant Measurements

Figures 27 - 29 show graphs of $[Br^-]/[Cl^-]$ vs. $[RBr]$ at 125°C for 18 of the alkyl bromides that were studied. In each graph, the linear regression of the points is also shown. From every graph, the slope of this line was used to determine k_{30} , the S_N2 reaction rate constant. The values for k_{30} for the alkyl bromides are reported in

Table 3 along with the relative reactivities of the compounds. The relative reactivity, RR , is calculated by Equation 38, and is a measure of the rate constant for a

$$RR = \frac{k_{30}(\text{RBr})}{k_{30}(\text{BE})} \quad (38)$$

particular RBR vs. that for BE. The values for RR are listed relative to BE to facilitate comparison with a compilation by Streitweiser (92) of relative solution-phase reactivities of alkyl halides. The uncertainty in k_{30} is 50-53%. It is determined primarily by the uncertainty in the estimation of $R_{+-}[P^+]$, and to a lesser extent by the uncertainty in the least squares fit of the data. The values determined for k_{30} and RR from Table 3 will be addressed at appropriate points in the discussion. For a few of the compounds, Table 3 lists experimental results from three different techniques (6, 14, 16) at three different pressures and two different temperatures.

Saturated Alkyl Bromides. The fourteen saturated alkyl bromides that were studied are abbreviated as follows: bromomethane (BM), bromoethane (BE), 1-bromopropane (1BPR), 1-bromobutane (1BB), 1-bromopentane (1BPE), 1-bromodecane (1BD), 2-bromopropane (2BPR), 2-bromobutane (2BB), 1-bromo-2-methylpropane (1B2MPR), 2-bromo-2-methylpropane (2B2MPR), 1-bromo-2,2-dimethylpropane (1B22DMPR), 1-bromo-3-methylbutane

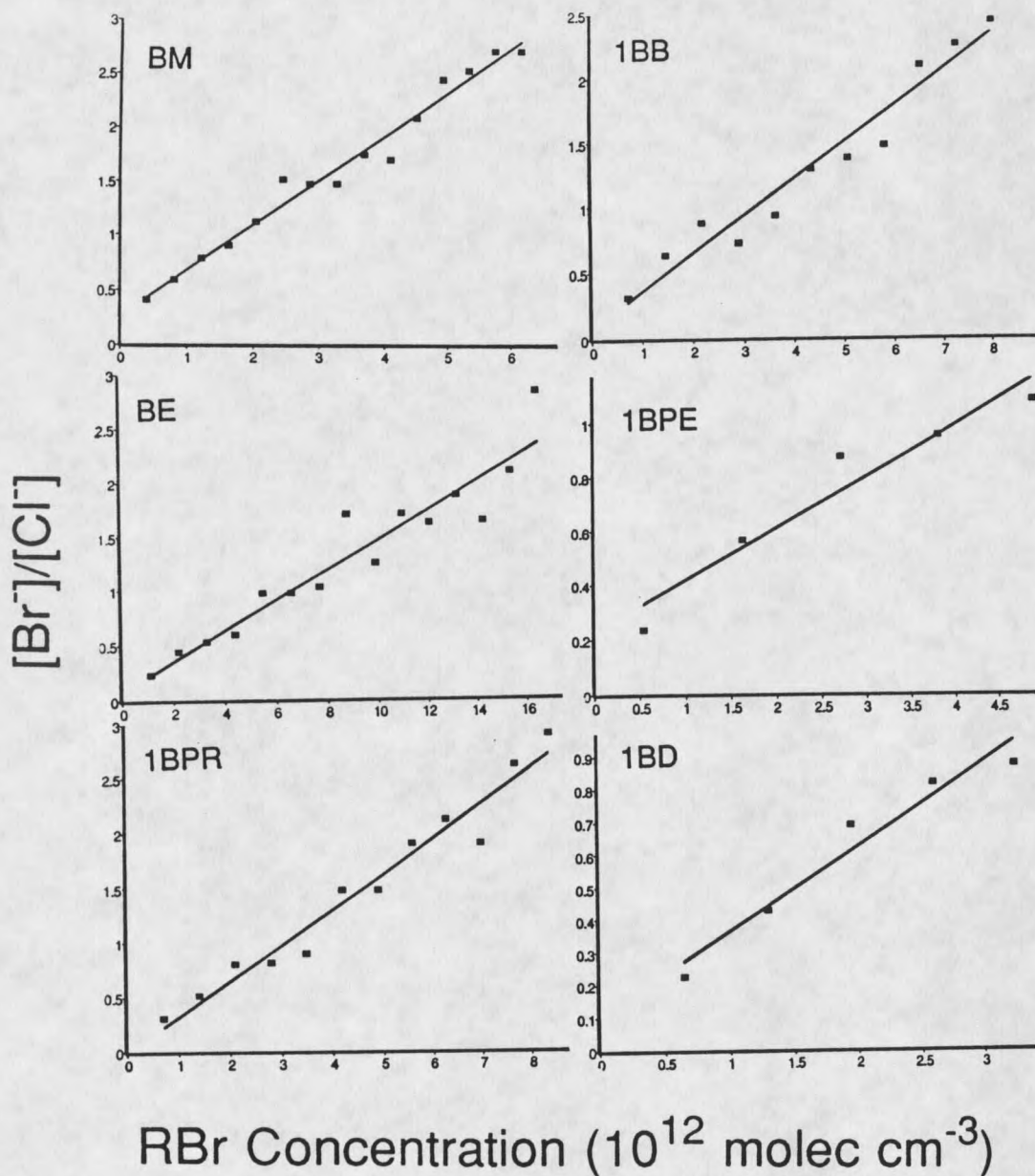


Figure 27.

Plots of ECD concentrations of RBr vs. $[\text{Br}^-]/[\text{Cl}^-]$ for six primary unsubstituted saturated alkyl bromides. The solid line is the least squares fit of the experimental data. The slope of this line corresponds to $k_{19}/R[\text{P}^+]$.

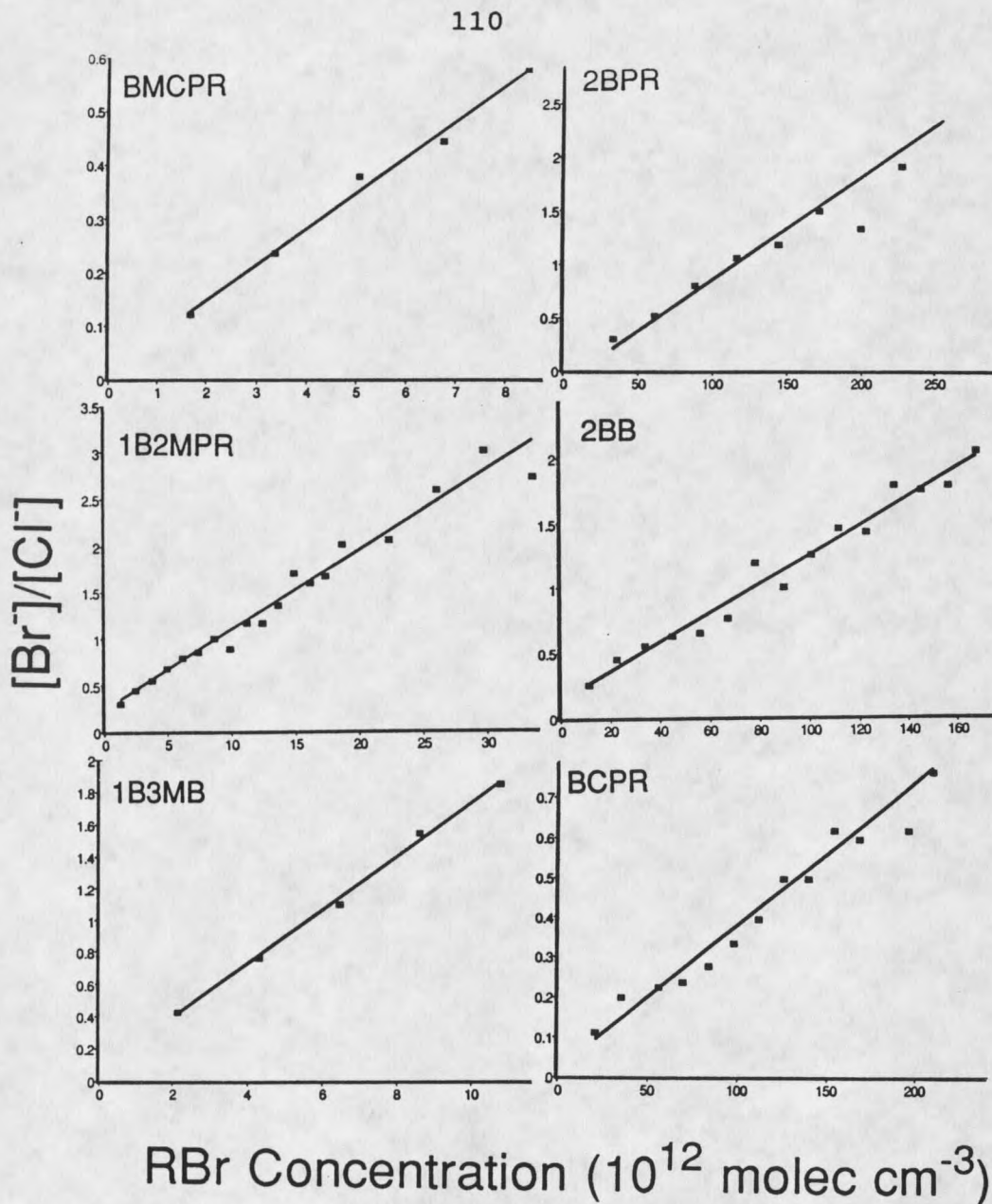


Figure 28.

Plots of ECD concentrations of RBr vs. $[Br^-]/[Cl^-]$ for three primary substituted and three secondary saturated alkyl bromides. The solid line is the least squares fit of the experimental data. The slope of this line corresponds to $k_{19}/R[P^+]$.

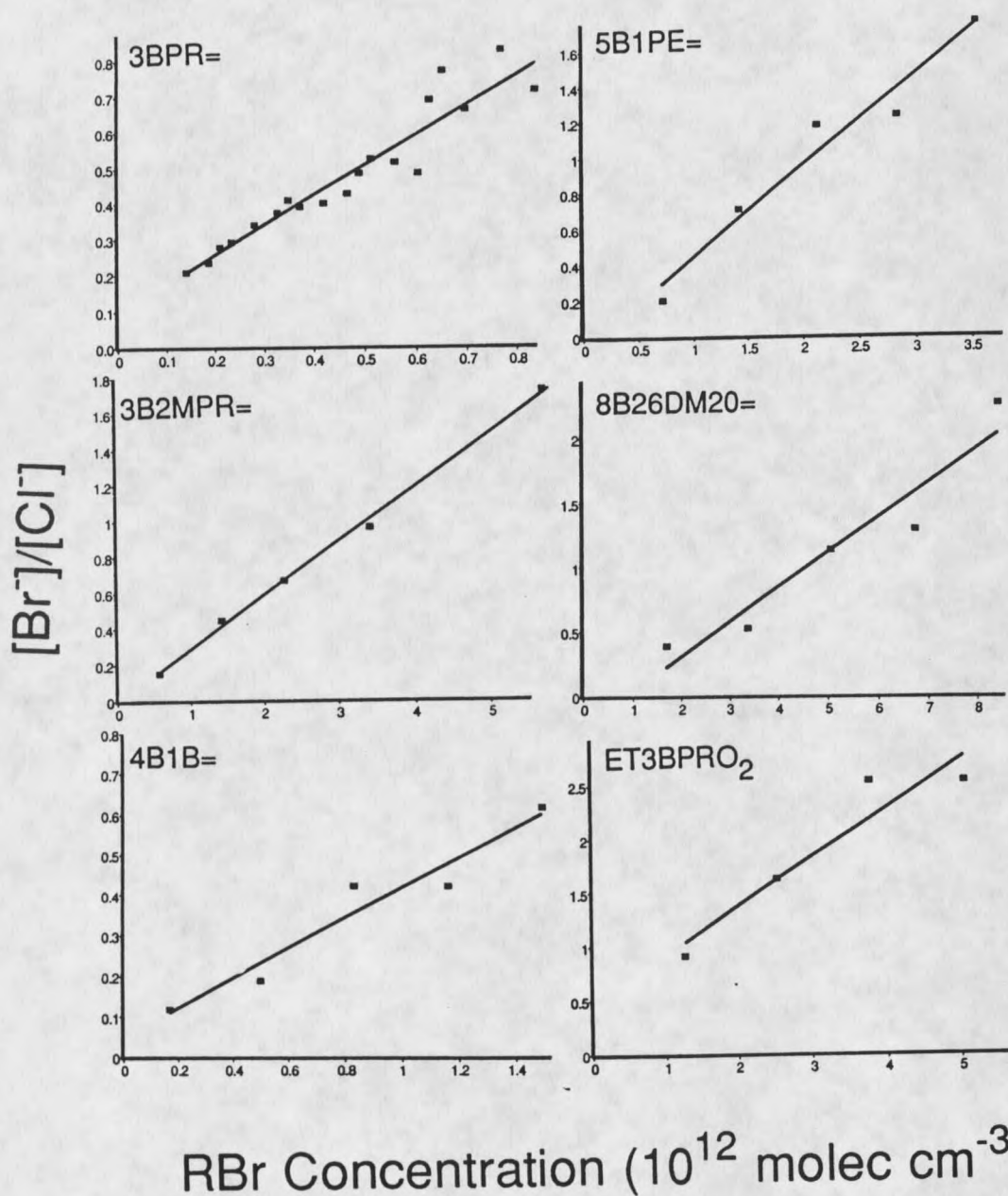


Figure 29.

Plots of ECD concentrations of RBr vs. $[Br^-]/[Cl^-]$ for six primary unsaturated alkyl bromides. The solid line is the least squares fit of the experimental data. The slope of this line corresponds to $k_{19}/R[P^+]$.

Table 3.

Rate Constants and Relative Reactivities for
 $\text{RBr} + \text{Cl}^- \longrightarrow \text{RCl} + \text{Br}^-$.

Compound	PDM-ECD ^a	KIMMS ^b	PHPMS ^c		FA-SIFT ^d	solution phase ^e
	(640 torr 125°C)	(640 torr 125°C)	(4 torr) 125°C	25°C	(0.5 torr 25°C)	
BM	4.1 ± 2.1 ^f (2.9) ^g	3.4 (2.8)	0.88 (0.91)	1.9 (3.3)	2.7 (5.4)	(30)
BE	1.4 ± 0.7 (1.0)	1.2 (1.0)	0.97 (1.0)	0.57 (1.0)	0.5 (1.0)	(1.0)
1BPR	3.2 ± 1.6 (2.3)				1.5 (3.0)	(0.4)
1BB	2.8 ± 1.4 (2.0)	2.2 (1.8)	2.0 (2.1)	2.0 (3.5)		(0.4)
1BPE	1.9 ± 1.0 (1.4)					
1BD	2.6 ± 1.3 (1.9)					
1B2MPR	0.85 ± 0.43 (0.61)					(0.03)
BMCPR	0.66 ± 0.33 (0.47)					
1B3MB	1.7 ± 0.8 (1.2)					
1B22DMPR	<0.0091 (<0.006)				<0.01 (<0.02)	(0.00001)
2BPR	0.097 ± 0.050 (0.069)	0.078 (0.065)	0.063 (0.065)	0.0048 (0.0084)	<0.01 (<0.02)	(0.025)
BCPR	0.036 ± 0.018 (0.026)					(<0.0000026)
2BB	0.11 ± 0.056 (0.079)					
2B2MPR	<0.22 (<0.16)				<0.01 (<0.02)	
3BPR=	8.4 ± 4.2 (6.0)					(40)
3B2MPR=	3.0 ± 1.5 (2.1)					

Table 3. (continued)

Compound	PDM-ECD ^a (640 torr 125°C)
4B1B=	3.7 ± 1.9 ^f (2.6) ^g
5B1PE=	5.1 ± 2.6 (3.6)
8B26DM2O=	2.7 ± 1.4 (1.9)
E3BPRO ₂	4.6 ± 2.5 (3.3)

^a Present work, from Figures 27 - 29.

^b KIMMS measurements from reference 6.

^c PHPMS measurements from reference 14.

^d FA-SIFT measurements from reference 16.

^e Solution-phase S_N2 relative reactivities for alkyl systems. The number listed is averaged for several different nucleophiles, leaving groups and solvents. From reference 92.

^f Rate constants in units of 10⁻¹¹ cm³ s⁻¹.

^g The ratio of the experimental rate constant to that for bromoethane ($k_{30(\text{RBr})}/k_{30(\text{BE})}$).

(1B3MB), bromocyclopropane (BCPR) and (bromomethyl)cyclopropane (BMCPR).

The reactions of a few of the alkyl bromides with chloride have been studied by many different researchers and by several different techniques in the gas phase. However, only two reports included measurements made at

the temperature used in this study, 125°C. The results from these two studies are included in Table 3 for comparison with the PDM-ECD measurements. In one of the studies, Giles and Grimsrud investigated the reactions of Cl^- with BM, BE, 2BPR, and 1BB at 640 torr and 125°C in a kinetic ion mobility mass spectrometer (KIMMS) (6). In the other study, Caldwell et al. used a pulsed e-beam high pressure mass spectrometer (PHPMS) to investigate the reactions of Cl^- with BM, BE, 2BPR, 1BB, and one other compound at 125°C and at a pressure of 4 torr (14). In the PHPMS study, there is some confusion as to the identity of one of the compounds because of several inconsistencies in the text. The compound is listed in the paper as isobutyl bromide (1B2MPR), a primary bromide, but is referred to in all instances as a secondary bromide. It is unclear whether the authors were indeed using 1B2MPR and were confused about its structure, or were using a secondary bromide and were mistaken about its name. Because of this uncertainty this compound was not included for comparison.

Examination of the rate constants for BM, BE, 2BPR, and 1BB in Table 3 reveals that there is good agreement between the measurements of k_{30} by KIMMS and by the PDM-ECD. This is not unexpected, since the reactions were carried out in similar environments by the two techniques.

It is observed, however, that the PDM-ECD measurements for the four compounds are uniformly larger by 17 - 27% than those from KIMMS. Although the difference between the two sets of results is within the relatively large uncertainty of the PDM-ECD measurements, it is important to consider a possible cause for the discrepancy, if it is real. Because the PDM-ECD results are all larger than those from KIMMS by a similar percentage, it is conceivable that the value for $R_{+-}[P^+]$, $100 \pm 50 \text{ s}^{-1}$, is slightly overestimated. If, for example, $R_{+-}[P^+] = 82 \text{ s}^{-1}$ were assumed, the calculations would yield excellent agreement between the two techniques.

When the values for k_{30} from the PDM-ECD are compared with those from PHPMS, fairly good agreement is obtained for BE, 2BPR, and 1BB. As before, the PDM-ECD measurements are uniformly larger than the PHPMS measurements, but not by more than the experimental uncertainty of the PDM-ECD technique. Again, if the discrepancy is systematic, it could be due to the estimation of $R_{+-}[P^+]$. Because of the agreement between the KIMMS and PHPMS results for BE, 2BPR, and 1BB; Giles and Grimsrud concluded that for these compounds, k_{30} is relatively independent of pressure over the range from 4 torr to 640 torr (6). The PDM-ECD measurements provide additional evidence for this conclusion.

From Table 3, the PDM-ECD value for k_{30} for BM is more than four times larger than the value from PHPMS. The KIMMS value for BM is also much larger than the PHPMS measurement. Giles and Grimsrud attribute the significant disparity in k_{30} to the pressure difference of more than two orders of magnitude between the two techniques (6). Because of the agreement with the KIMMS results for BM, the large PDM-ECD measurement is thought to be due to this same dependence on pressure.

The explanation of the pressure dependence of k_{30} for BM is aided by examination of the reaction coordinate for gas-phase S_N2 displacement, shown in Figure 30 (5). The general features of the reaction coordinate in Figure 30 correspond to the reaction of RBr with Cl^- . The relative energies of the wells and the transition state shown in the figure correspond to the specific case of BM (14). In general, the potential energy surface is thought to proceed from the reactants to an initial well corresponding to the formation of the ion-molecule complex, $Cl^- \cdot RBr$. This species then either passes over the concerted S_N2 transition state and rapidly forms products, or dissociates to the reactants. For a reaction of this type, k_{30} is determined by the Langevin/ADO collision rate constant, k_c , and the rate constants for the forward and back reactions, k_p and k_b , respectively

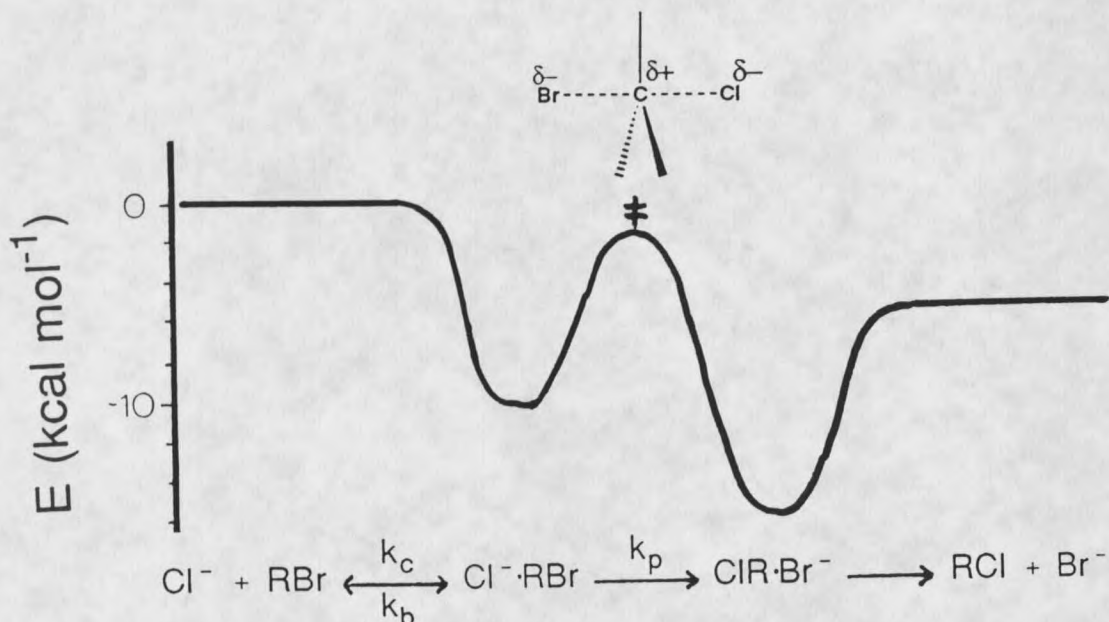


Figure 30.

Reaction coordinate for the $\text{S}_{\text{N}}2$ displacement reaction of Cl^- with RBr where $\text{R} = \text{CH}_3$. This reaction is thought to proceed first by formation of an intermediate ion-molecule complex, $\text{Cl}^- \cdot \text{RBr}$, and then by passage over a concerted transition state, \ddagger . In the transition state species, the carbon that is bonded to both Cl and Br bears a partial positive charge. Because of the rigid orientation requirements of the transition state species, the density of states at this point is thought to be low. The energies for the intermediates and transition state are from reference 14.

(5). The value for k_c is about $1.8 \times 10^{-9} \text{ cm}^3 \text{ s}^{-1}$ (for BM) and is calculated from Equation 15 (39) in Theory. The value for k_{30} is given by Equation 39 (5). Collisions of

$$k_{30} = \frac{k_c k_p}{k_p + k_b} \quad (39)$$

$\text{Cl}^- \cdot \text{RBr}$ with buffer gas molecules removes excess internal energy initially imparted to the species by the association of Cl^- and RBr (6). These thermalizing collisions occur more frequently at higher pressures. With the above discussion in mind, the disparity between the low and high pressure measurements of k_{30} for BM is attributed by Giles and Grimsrud to three factors. First, for the specific case of BM, the transition state is thought to be situated lower in energy than the reactants, as shown in Figure 30 (90). Second, the back reaction is thought to be entropically favored because the internal energy levels are more closely spaced for the loose orbiting transition state than for the "tight" $\text{S}_{\text{N}}2$ transition state (5). Third, Caldwell et al. observed that at 4 torr in the PHPMS, BM was never in thermal equilibrium with the buffer gas during the measurements of k_{30} (14). Giles and Grimsrud propose that at 640 torr, thermalization of $\text{Cl}^- \cdot \text{BM}$ is more complete than at 4 torr. Removal of excess internal energy from $\text{Cl}^- \cdot \text{BM}$ is thought to increase the entropically disfavored passage over the

tight transition state. This results in a larger ratio of k_p/k_b , and a corresponding increase in the observed k_{30} for BM (6). BE, 2BPR, and 1BB were observed to be in thermal equilibrium with the buffer gas in the PHPMS instrument (14), which explains the apparent pressure independence of k_{30} for these compounds.

It is well known that the structure of the substrate molecule in S_N2 displacement has a pronounced effect on the kinetics of the reaction. In particular, the effect of substrate alkylation on S_N2 reaction rates has been widely studied in the solution phase in a number of different solvents and for a variety of substrate-nucleophile systems. The relative reactivity, RR , is calculated by Equation 38 and should be useful in comparing the effects of structure on S_N2 kinetics for several gas-phase techniques and in the solution phase. The fourteen saturated alkyl bromides that were investigated by the PDM-ECD at 125°C vary widely in structural complexity, and this is reflected in their RR values shown in Table 3. In addition to the PHPMS and KIMMS results at 125°C which were discussed previously, Table 3 also includes a few gas-phase measurements by PHPMS at 25°C (14), and by a flowing afterglow-selected ion flow tube (FA-SIFT) instrument at 25°C (0.5 torr)

(16). Finally, solution-phase relative reactivities are also shown for several of the alkyl systems (92).

Several obvious and familiar trends are observed in the PDM-ECD data shown in Table 3. First, the PDM-ECD data shows that the RR for BM is larger than for the unsubstituted primary alkyl bromides. This result is mirrored in the solution phase, although the effect is greatly magnified. According to the traditional theoretical model, BM should be more reactive than the primary bromides because the α carbon bears no alkyl substituents to sterically hinder the approach of the nucleophile (82).

In light of the above discussion, it is interesting to compare the PDM-ECD RR for BM with the gas-phase RR by PHPMS at the same temperature. In contrast to the PDM-ECD result, the PHPMS measurement indicates that at 125°C, BM is less reactive towards S_N2 displacement than BE. This is thought to be due to two related factors. First, as explained above, the ratio of k_p/k_b for BM is expected to be larger at 640 torr in the PDM-ECD than at 4 torr in the PHPMS. Second, k_{30} for BM was observed to have a negative dependence on temperature in the PHPMS study, while BE showed a small positive temperature dependence (14). Therefore, it is not surprising that at the lower temperature of 25°C, the RR for BM is 3.3 and 5.4 by PHPMS

and FA-SIFT, respectively. In the gas phase, the initially formed $\text{Cl}^- \cdot \text{BM}$ complex contains less internal energy at higher total pressures and lower temperatures. Under conditions of lower energy, the reactivity of BM and other alkyl bromides towards $\text{S}_{\text{N}}2$ displacement is thought to be governed primarily by steric interactions.

Another interesting observation can be made from Table 3 with regard to unsubstituted saturated primary alkyl bromides. In the PDM-ECD, all of these compounds are more reactive than BE towards $\text{S}_{\text{N}}2$ displacement by Cl^- . The same result was seen in the gas phase by PHPMS and FA-SIFT for two of the compounds, 1BPR and 1BB. This suggests that a longer unsubstituted carbon chain on the α carbon does not sterically hinder the approach of the nucleophile. In the absence of steric effects, the slightly increased reactivity of the longer chain compounds relative to BE may be related to a greater ability of the longer alkyl groups attached to the α carbon to stabilize the transition state (82).

For primary alkyl systems, substitution at the β carbon is expected to cause a significant amount of steric hindrance in the approach of the nucleophile (82). This effect is clearly observed in both the gas- and solution-phase RR values for 1B2MPR and 1B22DMPR, and in the PDM-ECD result for BMCPR. In the case of 1B22DMPR, a rate

constant could not be measured in the PDM-ECD. At the high concentrations necessary to produce a PD response, a response due to EC was also observed. The extent to which Br^- was produced by either Reaction 30 or dissociative EC was therefore unclear. However, it was possible to estimate an upper limit for k_{30} from Equation 40, where N

$$k_{30} < \frac{N R_{+-} [\text{P}^+]}{[\text{Cl}^-]_0 [\text{RBr}]} \quad (40)$$

is the magnitude of baseline noise in the PD response and $[\text{Cl}^-]_0$ is the saturation level. The upper limits for k_{30} and RR are listed in Table 3. These values illustrate the well-known unreactivity of neopentyl systems toward $\text{S}_{\text{N}}2$ displacement (82).

Secondary alkyl systems have substantially reduced reactivities in $\text{S}_{\text{N}}2$ displacement because the α carbon bears two bulky substituents (82). This effect is seen in all of the gas- and solution-phase RR values for 2BPR and BCPR shown in Table 3 and in the PDM-ECD results for 2BB. Of all of the compounds that were studied, BCPR displayed the smallest measurable rate constant that was determined by the PDM-ECD. In the gas phase, the RR for BCPR is 100 times smaller than for BM. In the solution phase, $\text{S}_{\text{N}}2$ displacement is unmeasurably slow for cyclopropyl systems. According to Streitweiser (92), cyclopropyl halides are

extremely unreactive in displacement reactions because of their strained configuration.

In solution, tertiary halides react with nucleophiles almost exclusively by elimination (81). As was the case for 1B22DMPR, it was not possible to measure a rate constant for 2B2MPR in the PDM-ECD. Upper limits for k_{30} and RR were calculated from Equation 40 and are listed in Table 3.

Unsaturated Compounds. The six compounds with double bonds that were studied are as follows: 3-bromopropene (3BPR=), 3-bromo-2-methylpropene (3B2MPR=), 4-bromo-1-butene (4B1B=), 5-bromo-1-pentene (5B1PE=), 8-bromo-2,6-dimethyl-2-octene (8B26DM2O=), and ethyl-3-bromopropanoate (E3BPRO₂).

Unfortunately, S_N2 displacement has not been studied in the gas phase for any of the above unsaturated bromides. However, S_N2 displacement for similar systems has been studied in the gas phase and in solution. Of the unsaturated compounds, 3BPR= and 3B2MPR= are allylic systems, compounds with a β olefinic carbon. From Table 3, these compounds are observed to react about three times faster in the PDM-ECD than their saturated analogs, 1BPR and 1B2MPR. In addition, of all the compounds that were studied, 3BPR= exhibited the largest value for k_{30} . In a recent gas-phase report, DePuy et al. (16) reported a

similar enhancement using FA-SIFT. In that study, S_N2 reactions of H_2NS^- and HS^- with 3-chloropropene occurred significantly faster than with 1-chloropropane. In solution, it is also well-known that allylic systems have greatly enhanced S_N2 reactivity relative to saturated compounds (82, 92). From Table 3, the RR for allylic systems in solution is 100 times greater than for 1-propyl systems.

Two important factors are thought to contribute to the increased reactivity of 3BPR= and 3B2MPR= in the PDM-ECD study. The first factor has to do with stabilization of the transition state. In Figure 30, the α carbon at the transition state is bonded to both Cl and Br, and therefore bears a partial positive charge. In allylic systems, this charge is stabilized by the delocalized π molecular orbitals (82), and therefore, the energy of the transition state is thought to be lowered (92). The second factor in increased reactivity of allylic systems involves an additional nucleophilic displacement reaction available to these compounds. 3BPR= and 3B2MPR= can react with Cl^- by Reaction 41, the S_N2' reaction. In the S_N2' reaction, the nucleophile attacks the γ olefinic carbon and causes rearrangement of the double bond (82).

